Grant Agreement No: 101096307

Full Title: THz Industrial Mesh Networks in Smart Sensing and Propagation Environments

Start date: 01/01/2023

End date: 31/12/2025

Duration: 36 Months

Deliverable D3.3

Characterization of IRS, high directivity and beam steering antennas at sub-THz frequencies

Document Type	Deliverable
Title	D3.3
Contractual due date	30 June 2025 (M30)
Actual submission date	30 June 2025 (M30)
Nature	Report
Dissemination Level	PUB
Lead Beneficiary	CNRS
Responsible Author	G. Ducournau (CNRS)
Contributions from	Frédéric Dutin (CNRS), V. Torres (ANTERAL)

6GSNS

Revision history

Version	Issue Date	Changes	Contributor(s)
V0.1	12/06/2025	Initial version	G. Ducournau, F. Dutin (CNRS), V. Torres (ANT)
V0.2	28/06/2025	Revision of document after review by Per Hjalmar Lehne (Telenor) and Sébastien Chartier (IAF)	G. Ducournau, F. Dutin (CNRS), V. Torres (ANT)
V1.0	04/07/2025	Final review and acceptance	Luca Sanguinetti (CNIT), Thomas Kurner (TUBS)

Disclaimer

The content of the publication herein is the sole responsibility of the publishers, and it does not necessarily represent the views expressed by the European Commission or its services.

While the information contained in the documents is believed to be accurate, the authors(s) or any other participant in the TIMES consortium make no warranty of any kind with regard to this material including, but not limited to the implied warranties of merchantability and fitness for a particular purpose.

Neither the TIMES Consortium nor any of its members, their officers, employees or agents shall be responsible or liable in negligence or otherwise howsoever in respect of any inaccuracy or omission herein.

Without derogating from the generality of the foregoing neither the TIMES Consortium nor any of its members, their officers, employees or agents shall be liable for any direct or indirect or consequential loss or damage caused by or arising from any information, advice, inaccuracy, or omission herein.

Copyright message

© TIMES Consortium, 2022-2025. This deliverable contains original unpublished work except where clearly indicated otherwise. Acknowledgement of previously published material and of the work of others has been made through appropriate citation, quotation, or both. Reproduction is authorised provided the source is acknowledged.

Table of Contents

List of Abbreviations

AoA	Angle of Arrival
AoD	Angle of Departure
LoS	Line-of-Sight
NLoS	Non-Line-of-Sight
OTA	Over-the-Air
RS	Reflective Surface
RIS	Reconfigurable Intelligent Surface
THz	Terahertz
TRM	Thru, Reflect, Match
VNA	Vector Network Analyzer

Executive Summary

This document offers a brief overview of the characterization steps realized for the different free-space devices that were fabricated for THz transmission in the TIMES project. Antenna devices and reflective surfaces are covered in the report.

1. Introduction

1.1 Scope

This deliverable provides a summary of the characterizations done for the different antennas and reflective surfaces designed (as reported in the WP5 / D5.4) and fabricated in the TIMES project.

In TIMES, 2 Proof-of-Concept (PoC) demonstrations are targeted, including over-the-air (OTA) propagation. In these PoCs, OTA in the 300 GHz band is enabled by radiation of the signal using mainly two types of antennas: high-gain antennas and low-gain/beam steerable antennas, that were characterized and main conclusions are reported in this document. OTA transmission is also considering the use of IRS in the THz channel, requiring characterizations of the surfaces. This last item is also part of this deliverable.

1.2 Audience

This Report is intended for primary use by the TIMES Consortium and public dissemination.

1.3 Structure

The rest of the document is structured as follows:

- Section 2 presents the IRS characterization methods and results.
- Section 3 synthetizes the main outcomes of the antenna performances and results, for both high gain and beam-steering antennas.
- Section 4 presents the main conclusions

2 Reflective surface (RS) OTA (Over the Air) characterizations

2.1 RS first prototype

2.1.1 Description of the experimental setup

At CNRS, the performance characterization measurements in free space with a 220-325 GHz VNA of the passive RIS (or RS: reflective surface) were conducted.

Figure 1(a) shows the RS during these measurements. The RS is fixed onto a first rotating platform. The incident port of the VNA is in a fixed position while the reflected port is placed on a breadboard coupled to a rotating platform. Both rotating platforms have a rotation range of $360°$. With this configuration, they can be adjusted independently and we used them manually during acquisitions. To achieve the required THz alignments, both rotation stages have the same rotation axis. In the following, both sides of the RS are used. the front side is the frequency-dependent RS, and the backside is composed of pure metal and will be used as reference.

First, the VNA is calibrated using waveguide standards, using the TRM (Thru, Reflect, Match) method [2]. Doing so, the calibration plane is then set at the output of the VNA which is a metallic hollow-core waveguide in the 220-330 GHz range (WR3.4) (cf. Fig. Figure 1(a)). Then, over-the-air (OTA) measurements are enabled by connecting horn antennas at both VNA outputs. These standard horns are connected on each port of the VNA and are at the same height as the center of the RS. In order to illuminate the RS with known k-vector direction, the beams are collimated by using two THz lenses. These lenses (diameter 25 mm, focal length 25 mm) are placed in front of horn antennas. The distance between horn and lens is adjusted to get the lens focal point corresponding to the phase-center of each horn antenna. The collimated beam is then illuminating the RS, deflected and collected again by the second lens (L2). The distance between the lenses and the RS is about 125 mm, and the 2 distances were set to be almost identical.

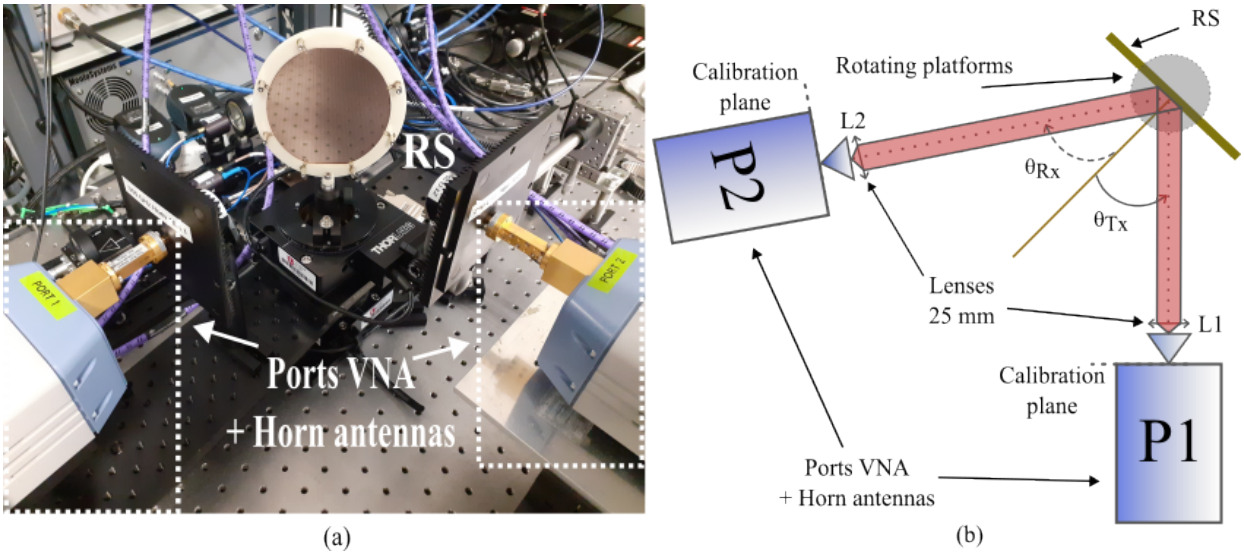

Figure 1. (a) Photo and (b) drawing of the VNA experimental setup.

The antenna gains over the WR3.4 band were checked prior to experiment. For this, the two identical horns are aligned and gain calculated from S_{21} and the usual Friis equation. The typical gain is shown in Figure 2.

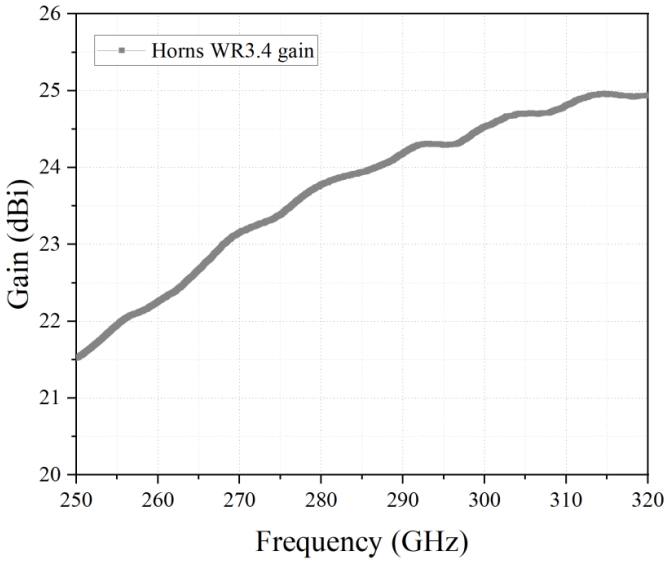

Figure 2. Horn antenna gain (Horn input is a WR3.4 waveguide).

In Figure 1(b), θ_{AOA} and θ_{AOD} are the angle of arrival and the angle of departure with respect to the normal of the RS, respectively. Angles are adjusted using rotation stages with a 5° step (identical for θ_{AOA} and θ_{AOD}) and are swept from 0° to 45° for θ_{AOA} and from 20° to 70° for θ_{AOD}. According to the testbed configuration, the specular reflection can be measured for $\theta_{\mathrm{AOA}} = \theta_{\mathrm{AOD}}$ from 20° to 45°, enabling to assess the impact of the incident angle on RS's absorption bandwidth discussed in the next section. Then we measured the S_{21} parameter for all different angles combinations $(\theta_{\mathrm{AOA}}, \theta_{\mathrm{AOD}})$ which are noted in Table 1. Gray cells correspond to specular configurations, where $\theta_{\mathrm{AOA}} = \theta_{\mathrm{AOD}}$. As shown in Table 1, we did 36 measurements for both RS and metallic backside of the RS for reference. For each value of θ_{AOD}, we rotated the RS to change θ_{AOA} and acquired the S_{21} amplitude and phase.

Table 1. Couple of angles for insertion loss measurements. Gray cells correspond to specular configurations

$(\boldsymbol{\theta_{\mathrm{AOA}}, \theta_{\mathrm{AOD}}})$					
$\mathbf{(20, 20)}$	(25,25)	(30,30)	(35,35)	(40,40)	(45,45)
$\mathbf{(15, 25)}$	(20,30)	(25,35)	(30,40)	(35,45)	(40,50)
$\mathbf{(10, 30)}$	(15,35)	(20,40)	(25,45)	(30,50)	(35,55)
$\mathbf{(5, 35)}$	(10,40)	(15,45)	(20,50)	(25,55)	(30,60)
$\mathbf{(0, 40)}$	(5,45)	(10,50)	(15,55)	(20,60)	(25,65)
$\mathbf{(-5, 45)}$	(0,50)	(5,55)	(10,60)	(15,65)	(20,70)

2.1.2 RS bandwidth analysis using specular response analysis

First, we compared S_{21} amplitudes of specular reflections for the RS and for the metallic plate (RS back-side) for different incident angles. Before any interpretations, the curves we measured were particularly affected by standing wave due the quasi-optic configuration rather than induced by the RS. Thus, we smoothed all of them by using a Savitzky-Golay filter of degree 3 where the span is about 20 points for a 5 GHz spectral range to obtain Figure 3(a)-(f) and Figure 4(a)-(e).

In Figure 3(a)-(f), we note that in the specular case, the metal plate and the RS got almost the same S_{21}. Thus, the RS is not absorbing anything between 220-270 GHz and 315-325 GHz (mirror-like behavior). Nevertheless, from 270 GHz to 315 GHz, for each incident angle, we have a clear absorbing behavior with a decreased S_{21} up to a 15 dB absorption level. However, the incident angle seems to play a role related to the width of

absorbed frequency (AF) range. In the proposed method, the determination of the RS absorbing frequency range in the specular case provides the basis of the next analysis which focus on the nonspecular behavior of the RS. Indeed, the RS nonspecular operation frequency bandwidth should correspond to the RS specular absorption band, which is to be determined prior to the nonspecular analysis.

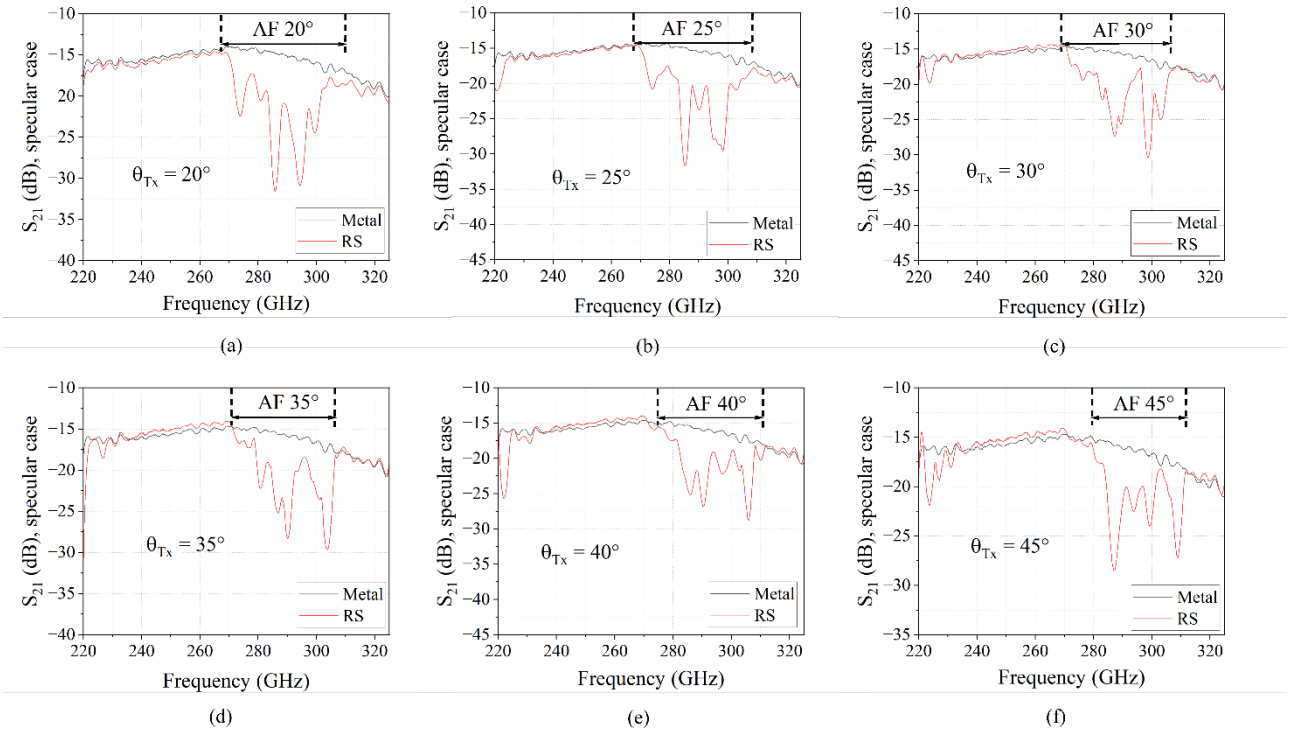

Figure 3. S_{21} amplitudes for specular reflections ($\theta_{AOA} = \theta_{AOD}$) configuration for the RS (red) and for the backside metallic plate (black) for (a) $\theta_{AOA} = 20°$, (b) $25°$, (c) $30°$, (d) $35°$, (e) $40°$ and (f) $45°$. The identified absorbed frequencies (AF) bandwidths in this figure show the frequency region where the RS is absorbing in the specular case.

2.1.3 Frequency band of the RS in the nonspecular case

The nonspecular S_{21} curves displayed in Figure 4(a)-(e) enable to compare RS nonspecular reflections with the metal plate specular reflection. Regarding these nonspecular reflections, two distinct patterns occur. A "quasi-specular reflection" is observed when θ_{AOA} and θ_{AOD} are close to each other (about $10°$) and a clear nonspecular reflection when angles are further from each other. Outside the RS bandwidth (270-315 GHz), a 40 dB decrease occurs for $\theta_{\mathrm{AOA}} = 20°$ between 220 and 260 GHz. In the RS bandwidth, the amplitude of the S_{21} is progressively increasing with incident angle, reaching its maximum of about -20 dB for angles $(\theta_{\mathrm{AOA}}, \theta_{\mathrm{AOD}}) = (20°, 60°)$. It confirms the RS bandwidth determined in the specular experiments.

In addition, we can clearly see the effect of moving the Rx antenna with respect to the RS. For instance, for $\theta_{\mathrm{AOA}} = 20°$, when θ_{AOA} increases we first observe a decrease of S_{21} magnitude (red and blue curves) then an increase (green and purple curves) and eventually a decrease (orange curve). Thus, in nonspecular case, we have, for each θ_{AOA}, a maximum of S_{21} for one θ_{AOD} when the angular configuration is optimal, corresponding to the optimal non-specular reflection on the RS. When the angular configuration is not optimal, a lower S_{21} is observed, which corresponds to a sub-optimal reflection case. We also observe in Figure 4(a) and (b) that for incident angles larger or equal than $15°$ and less than $30°$ we have a $40°$ shift

between specular and nonspecular reflections. Besides the quasi-specular reflection which always follows the specular one, we usually have a minimum at roughly $\theta_{\mathrm{AOD}} = 40°$ and a maximum 20° more.

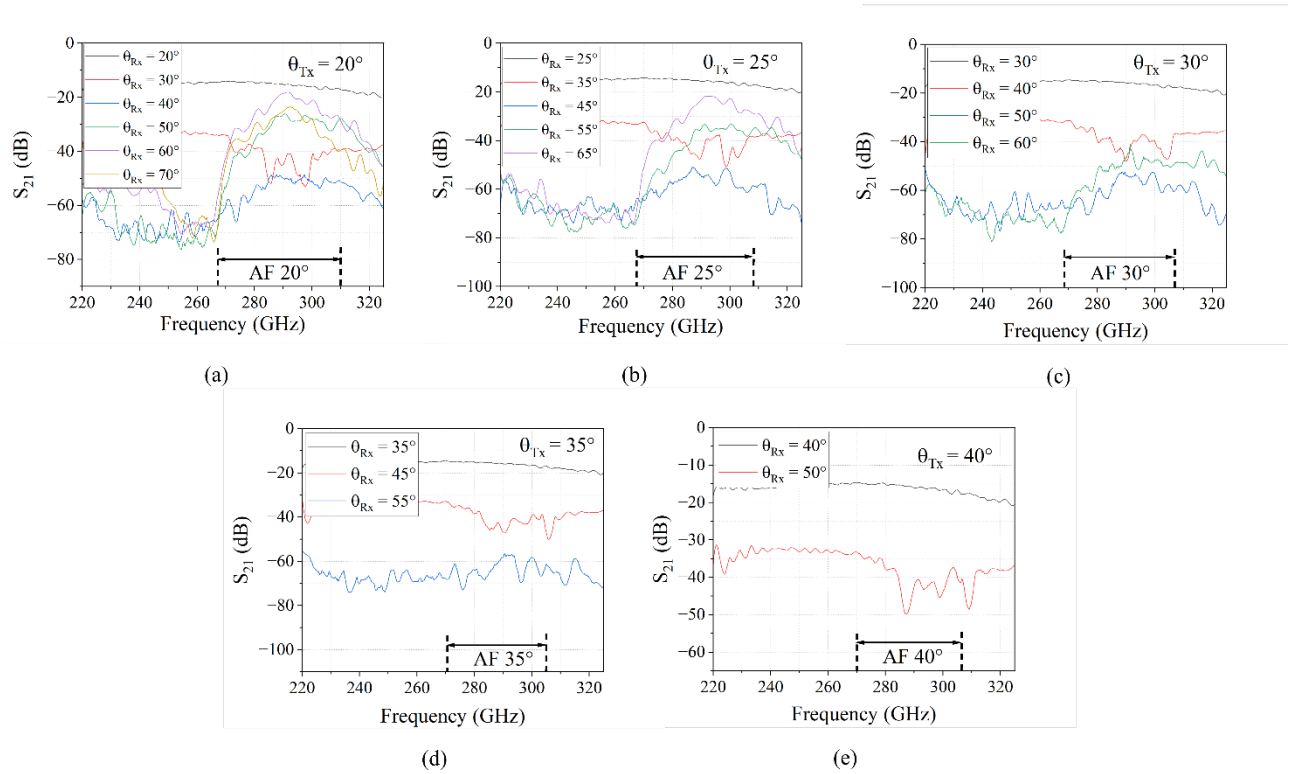

Figure 4. Comparison between S_{21} for a metallic plate specular reflection (black) and nonspecular reflections from a RS (other colors) for (a) $\theta_{AOA} = 20°$, (b) 25°, (c) 30°, (d) 35°, (e) 40°. The indicated bandwidth corresponds to the absorbed frequency (AF) range in the specular mode, see Figure 3, this frequency being then non-specularly radiated from the RS.

2.1.4 Determination of the RS losses

As displayed in Figure 5, we zoomed on the measured S_{21} specular reflection obtained with the metallic plate (RS backside) and the highest level obtained for nonspecular reflection from the RS was reached for angles $(\theta_{\mathrm{AOA}}, \theta_{\mathrm{AOD}}) = (20°, 60°)$ between 280 and 300 GHz. The minimum loss induced by the RS is then the relative amplitude shift between the two S_{21} curves. It is found that, related to the metal plate, the lowest RS loss is about 3 dB and occurs at about 290.6 GHz. The total RS bandwidth (@3dB) is found to be about 10 GHz. However, when using the RS inside a THz data-link with a wideband signal (modulated THz data), the overall loss induced by the RS corresponds to the averaged S_{21} over the signal bandwidth, that is close to 5 GHz (see section IV). Considering the bandwidth of the modulated spectrum in Figure 5 the expected loss is about 4 dB. A small shift of the carrier frequency was considered during measurement of the RS, as the testing system was achieving better performances at 292 GHz.

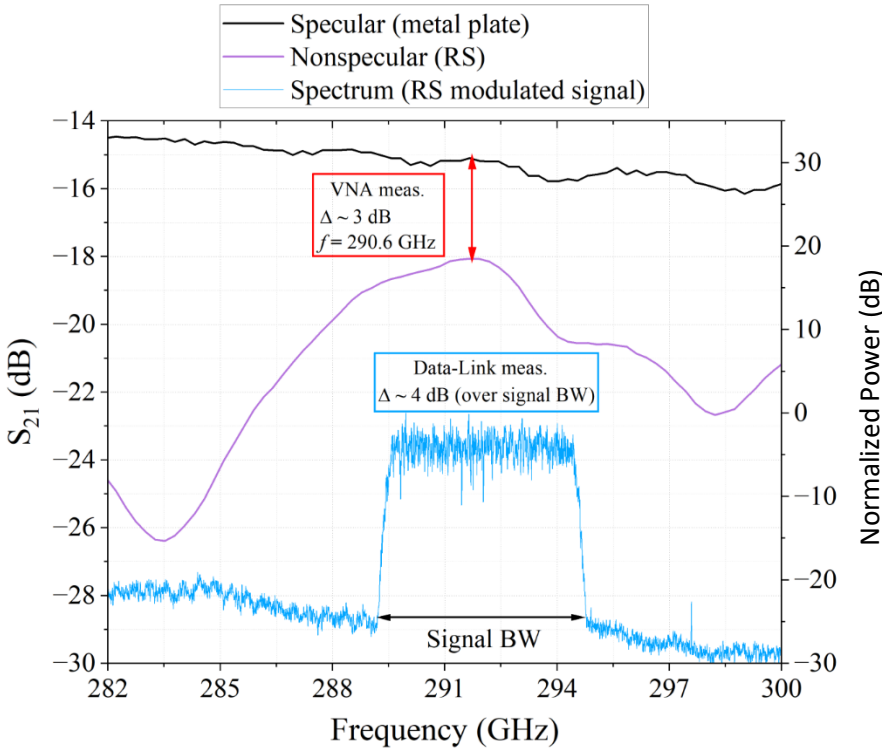

Figure 5. Zoom on the smallest measured shift between specular reflection S_{21} from the metallic plate and the nonspecular reflection one from the RS which occur for $\theta_{AOA} = 20°$ and $\theta_{AOD} = 60°$. The normalized power of the signal spectrum is shown (dB).

2.2 RS second prototype

2.2.1 Experimental setup description

To characterize this new RS, we used the same setup as for the first one and depicted in the Figure 1 (a). The Figure 6 shows the new RS on the experimental setup.

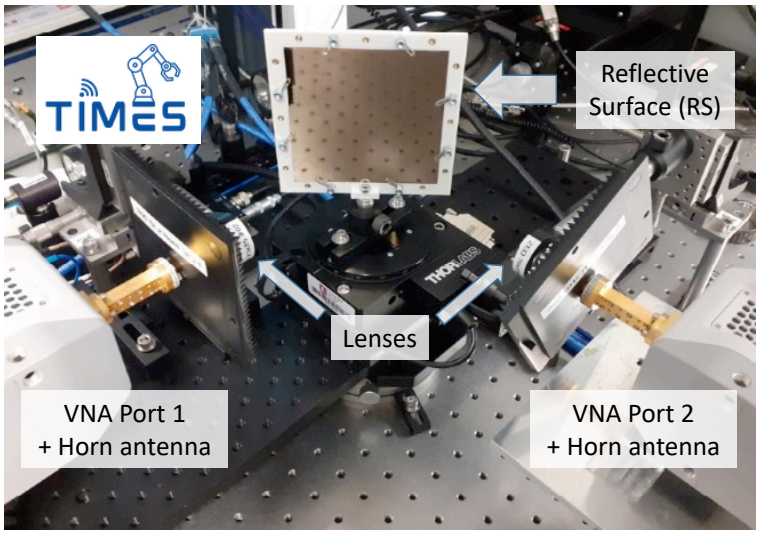

Figure 6. Photo of the VNA experimental setup for OTA characterization of the RS at 300 GHz.

In this work, we used the same experimental setup as for the one used for the RS first prototype; then, we refer the reader to the last section for everything to experimental setup.

As before, θ_{AOA} and θ_{AOD} are angle of arrival and angle of departure with respect to the normal of the RS, respectively but this time, angles are adjusted by using rotation stages with a 2° step (identical for θ_{AOA} and θ_{AOD}) and are swept from 0° to 44° for θ_{AOA} and from -4° to 70° for θ_{AOD}. According to the testbed configuration, specular reflection can be measured for $\theta_{\mathrm{AOA}} = \theta_{\mathrm{AOD}}$ from 20° to 44°, which enables to assess on the angle of arrival impact on the RS frequency bandwidth, as discussed in the next section. Then, the S_{21} parameter is measured for a large number of couples $(\theta_{\mathrm{AOA}}, \theta_{\mathrm{AOD}})$ which correspond to 13 different angles of arrival and 26 different angles of departure, or 338 acquisitions for the RS and for the metal plate as reference. For each value of θ_{AOA}, we rotate the reflected VNA port to change θ_{AOD} to measure amplitude and phase of S_{21}.

2.2.2 RS bandwidth analysis by specular reflection analysis

First, S_{21} amplitudes are compared for RS specular reflections and metal plate specular reflections (RS backside serving as reference) as well for different angles of arrival.

In Figure 7, we note, in the case of $\theta_{\mathrm{AOA}} = \theta_{\mathrm{AOD}} = 34°$, that in the specular case, the RS S_{21} only differ from metal plate between 271 GHz and 296 GHz which can be denoted as an absorption frequency (AF) range. Indeed, a clear absorbing behavior is obtained considering the S_{21} showing a large reduction of up to 34 dB. The AF range seems not to show any dependence on the AoA even though the absorption level is increasing from 15 dB ($\theta_{\mathrm{AOA}} = 20°$) to 40 dB for $\theta_{\mathrm{AOA}} = 44°$. To be more quantitative, for a given AoA, a major part of the absorbed signal in the specular configuration should reach an AoD in the nonspecular configuration (cf. Figure 8). Then, the AF range can be considered as the frequency band for which 90% of the absorbed signal flows out from the RS in a non-specular case. Fixing this criterion, the AF range is found to exceed 7 GHz for $\theta_{\mathrm{AOA}} = 34°$. Based on this preliminary analysis of the specular behavior of the RS, the next section details the RS bandwidth analysis of the non-specular reflection.

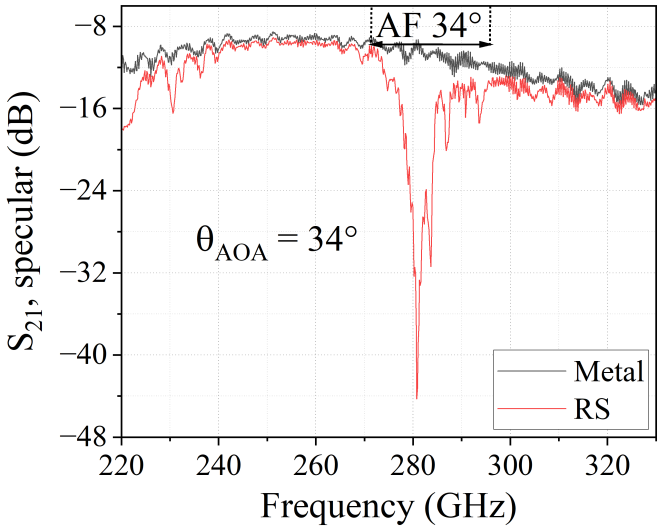

Figure 7. Example of S_{21} amplitude for specular reflection ($\theta_{AOA} = \theta_{AOD}$) configuration for the RS (red) and for the backside metallic plate (black) for $\theta_{AOA} = 34°$.

2.2.3 RS bandwidth analysis by non specular reflection analysis

S_{21} curves in the nonspecular case are displayed in Figure 8 and enable to compare RS nonspecular reflections and specular reflection. Outside of the RS bandwidth (271-296 GHz), a 60 dB decreasing is occurring, for instance, for $\theta_{\mathrm{AOA}} = 34°$ between 220 and 260 GHz. Within the RS bandwidth, S_{21} amplitude is progressively increasing with angle of departure and reach is maximum of about -13 dB for the couple

$(\theta_{\mathrm{AOA}}, \theta_{\mathrm{AOD}}) = (34°, 6°)$ at $f = 281.2$ GHz. This confirms the RS bandwidth determined by specular configuration experiments of the previous section.

It is also important to notice that when the angles of arrival are between 20° and 30°, the maximum of S_{21} occurs at roughly $f = 287$ GHz whereas for angles of arrival between 32° and 44°, it occurs at roughly $f = 281$ GHz (cf. Figure 9).

In the nonspecular case, we have, for each θ_{AOA}, a maximum of S_{21} for a specific θ_{AOD} when the angular configuration is optimal, which is corresponding to an optimal RS nonspecular reflection. As a contrary, when the angular configuration is not optimal, a weaker S_{21} is observed, which is corresponding to a sub-optimal nonspecular reflection. In Figure 9, the maximum of S_{21} as a function of the angle of arrival is shown for $\theta_{\mathrm{AOA}} = 34°$ at $f \approx 281$ GHz. Both maxima of S_{21} are clearly seen for $\theta_{\mathrm{AOA}} = 34°$ which corresponds to the specular case and for $\theta_{\mathrm{AOD}} = 6°$ which corresponds to the best angular configuration in the nonspecular case. We thus observe a roughly a $-30°$ shift between specular case and best nonspecular case angular configurations. More generally, when the angle θ_{AOA} is between 20° and 30°, this shift is close to $+40°$ whereas for θ_{AOA} between 32° and 44° the shift is more about $-30°$. Simulations were also performed and from the Floquet theory we can conclude that $+40°$ and $-30°$ shifts are related to $n = +1$ et $n = -1$ Floquet modes, respectively. In that sense, experimental results agree well with simulations. Even though, it has been observed in the simulations that for AoA $> 30°$, the structure's performance degrades because the unit cell design is intended for normal incidence (AoA $= 0°$). The presence of two modes in these measurements is in contrast with the previous RS prototype on which only the mode $n = +1$ was excited.

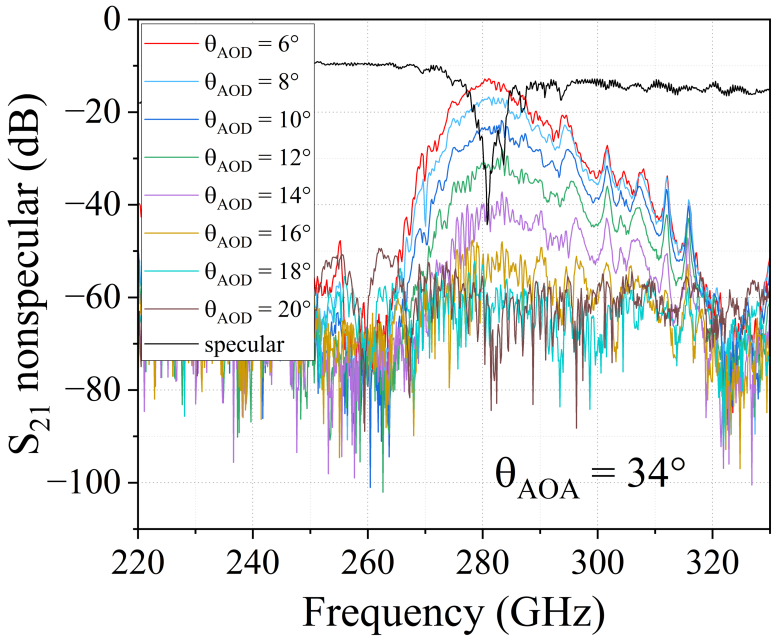

Figure 8. Comparison of S_{21} for the RS in specular reflection (black) and nonspecular reflections (other colours) for $\theta_{AOA} = 34°$.

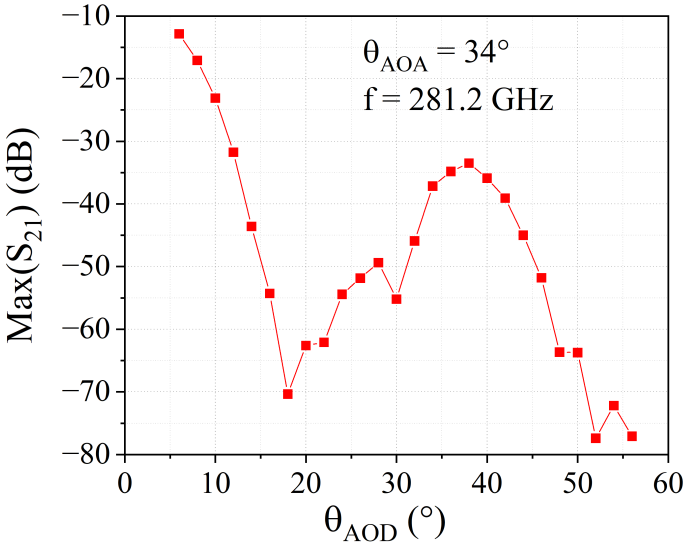

Figure 9. Evaluation of the maximum of S_{21} in terms of the angle of departure for $\theta_{AOA} = 34°$. We focused ourselves at $f = 281.2$ GHz which is the best nonspecular operation observed (maximum of S_{21}).

2.2.4 RS losses determination

Figure 10 shows a zoom of the measured S_{21} specular reflection obtained with the metallic plate (RS backside) and the maximum of S_{21} obtained for nonspecular reflection from the RS (cf. Figure 8) between 271 and 296 GHz (AF range). It is reached for $(\theta_{\mathrm{AOA}}, \theta_{\mathrm{AOD}}) = (34°, 6°)$ The minimum loss induced by the RS is thus the relative amplitude shift between the two curves. It then shows that, related to the metallic plate, the lowest RS loss is about 1.5 dB and occurs at about 281 GHz. The obtained results can be compared with the results from the first prototype, where the RS design was different in terms of periodicity and organization of unit cells. For instance, in the specular case, the AF band and the absorption bandwidth are shorter with this new design and the S_{21} amplitude decrease is higher and depends on the angle in this case. In the nonspecular case, RS losses are less and the shift between the angle in the specular case and the best angular configuration now depends on the angle of arrival.

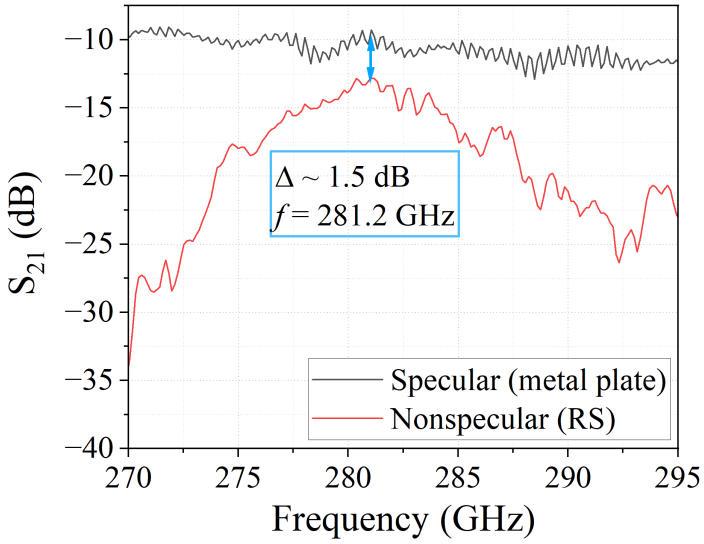

Figure 10. Zoom on the smallest measured shift between specular reflection S_{21} from the metal plate and the nonspecular reflection from the RS which occurs for $\theta_{AOA} = 34°$ and $\theta_{AOD} = 6°$.

3 Antenna characterization

3.1 High directivity antennas

The measurements of high directivity antennas are carried out in Anteral's characterization laboratory using a Keysight PNA-X N5242B vector network analyzer.

The prototype to be measured is connected to a frequency extender head from VDI, capable of transmission and reception in the 220 GHz to 330 GHz band. A near-field probe, also manufactured by Anteral, is used as the receiver, connected to another frequency extender head with reception-only capability.

The measurement process is divided into two steps:

1. A one-port calibrated measurement to assess return losses (S11) and verify the antenna's impedance matching in terms of delivered power.
2. A planar field measurement covering an area of 220 x 220 mm with a 2 mm step, corresponding to 0.45λ. This area is defined by a drop of more than 30 dB relative to the maximum. With this magnitude and phase measurement at each point of the planar field, the far-field radiation pattern can be calculated [1]. This mathematical calculation has been developed internally at Anteral.

The following images show several photographs of the measurement setup.

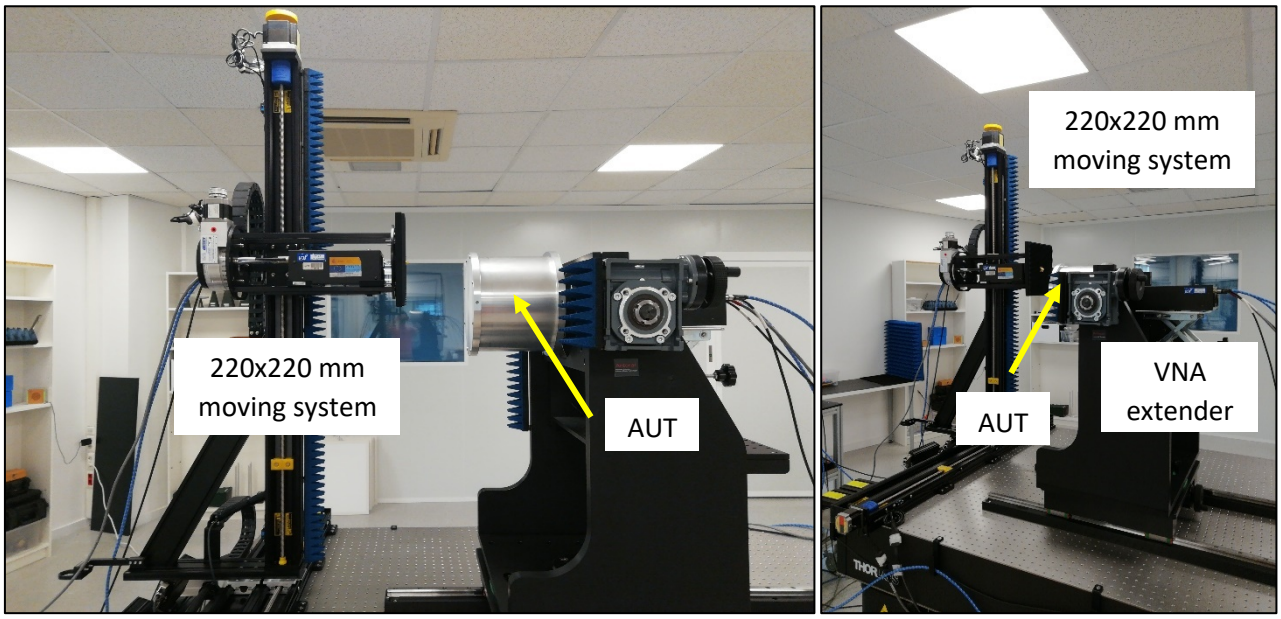

Figure 11. Measurement set-up for antenna measurement.

Below, the results of the first manufactured prototype, identified as SN4641, are presented first, followed by those of the second prototype, identified as SN5248.

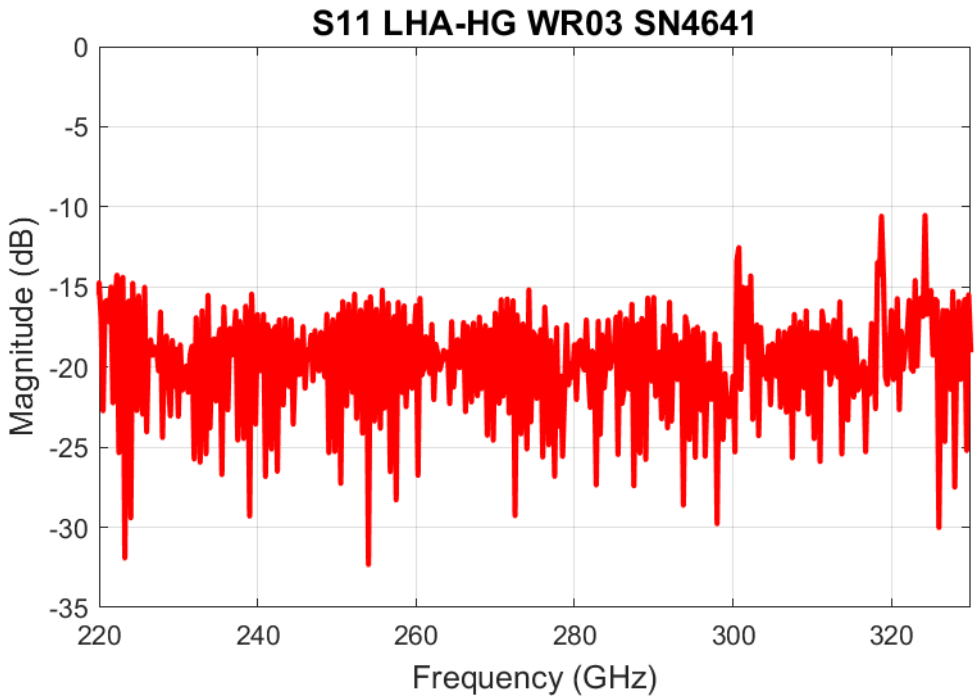

Figure 12. Measured S11 of prototype 1.

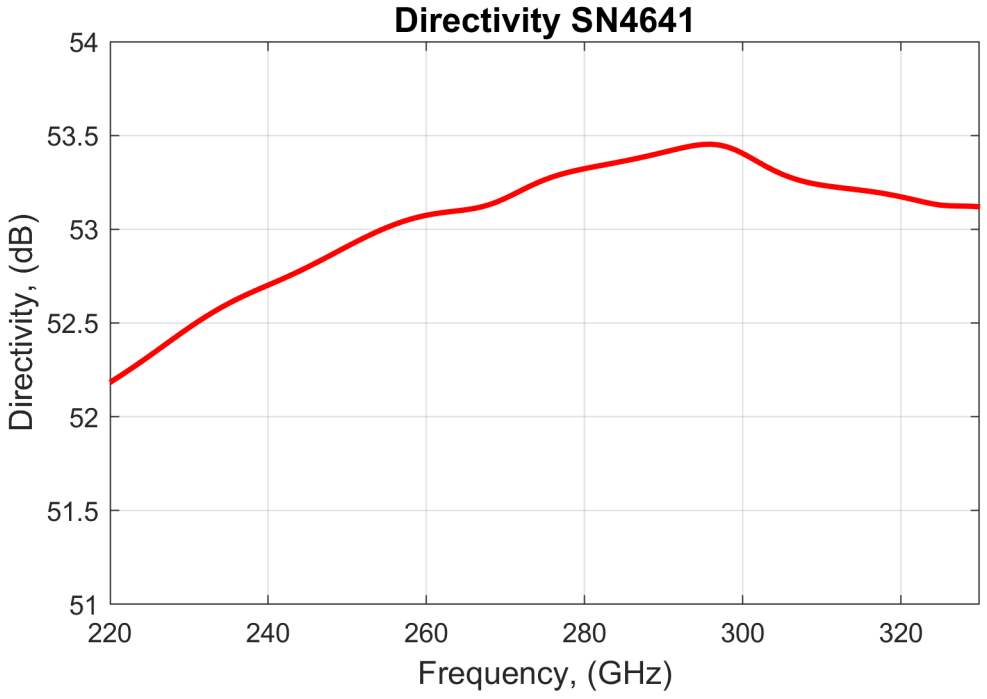

Figure 13. Measured directivity of prototype 1.

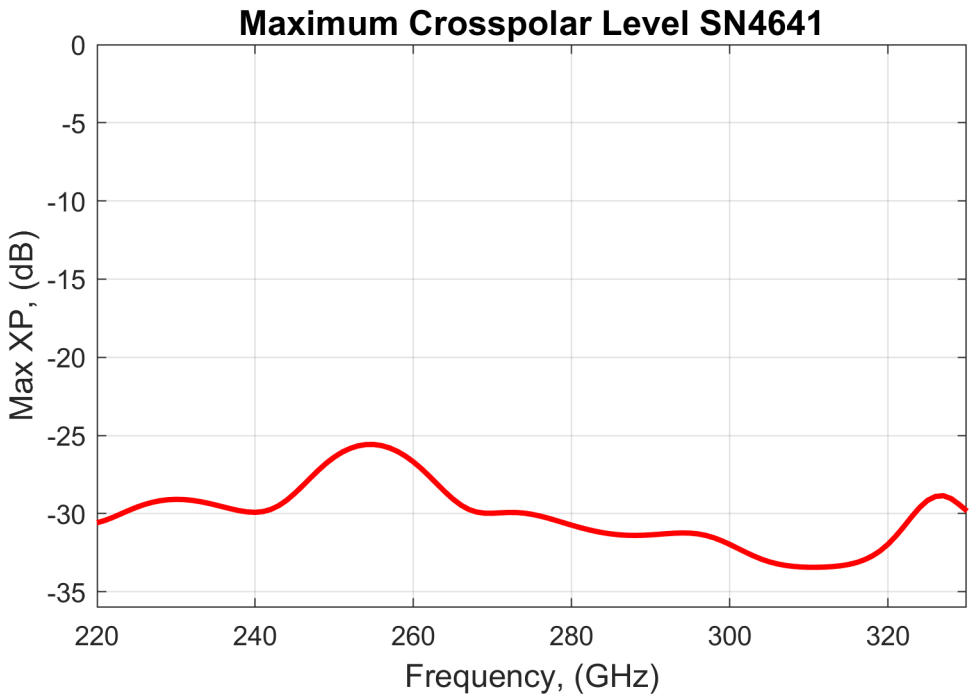

Figure 14. Max. measured crosspolar level of prototype 1.

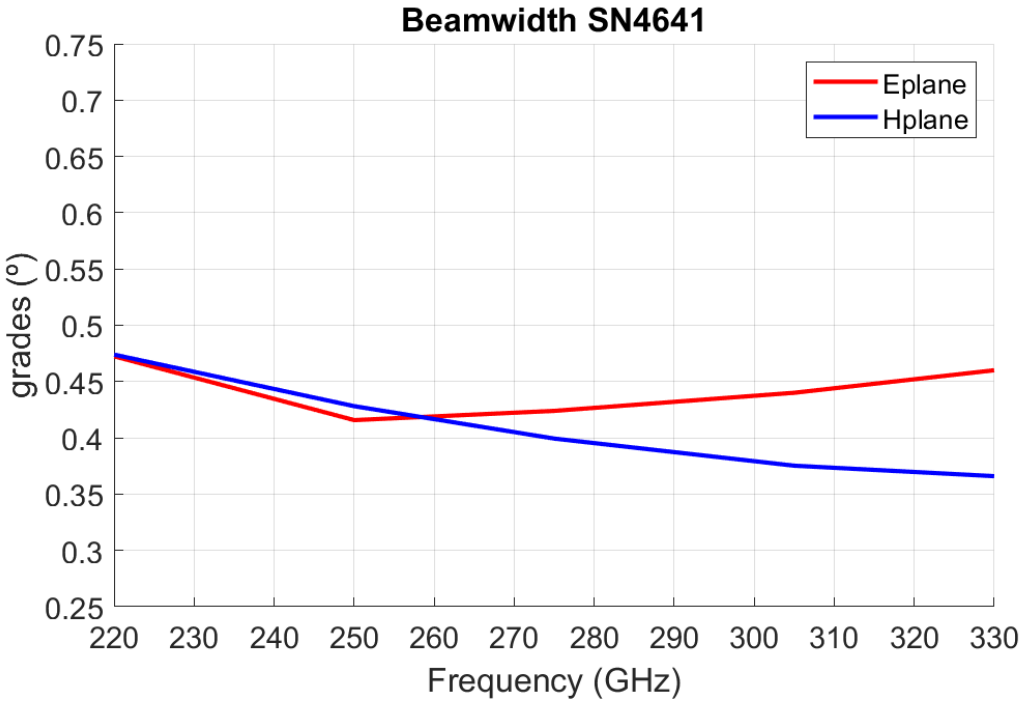

Figure 15. Beamwidth measured of prototype 1.

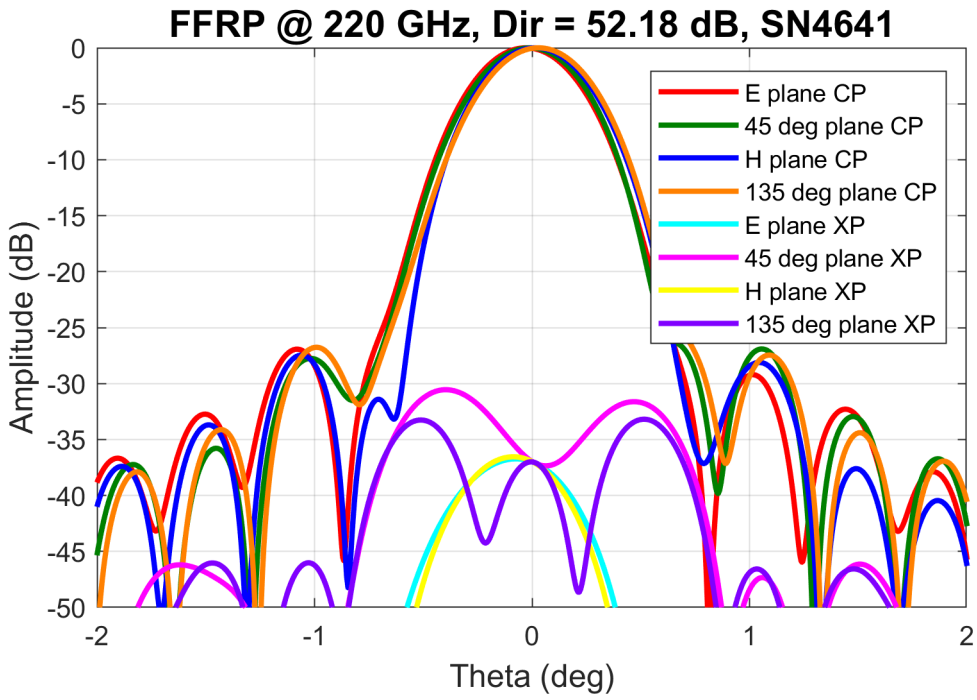

Figure 16. Measured far field radiation pattern at 220 GHz of prototype 1.

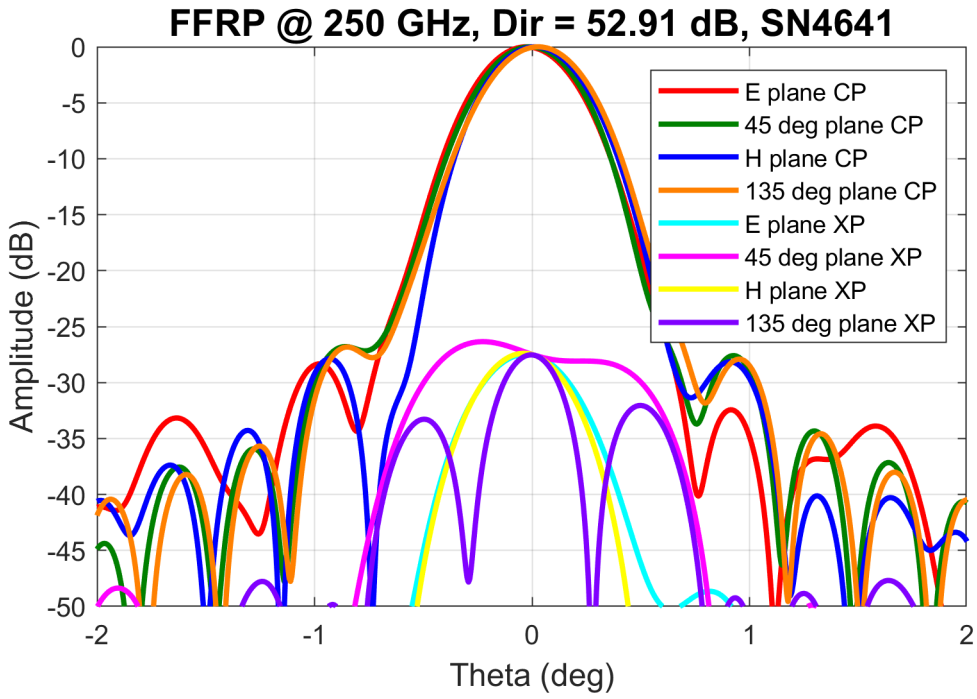

Figure 17. Measured far field radiation pattern at 250 GHz of prototype 1.

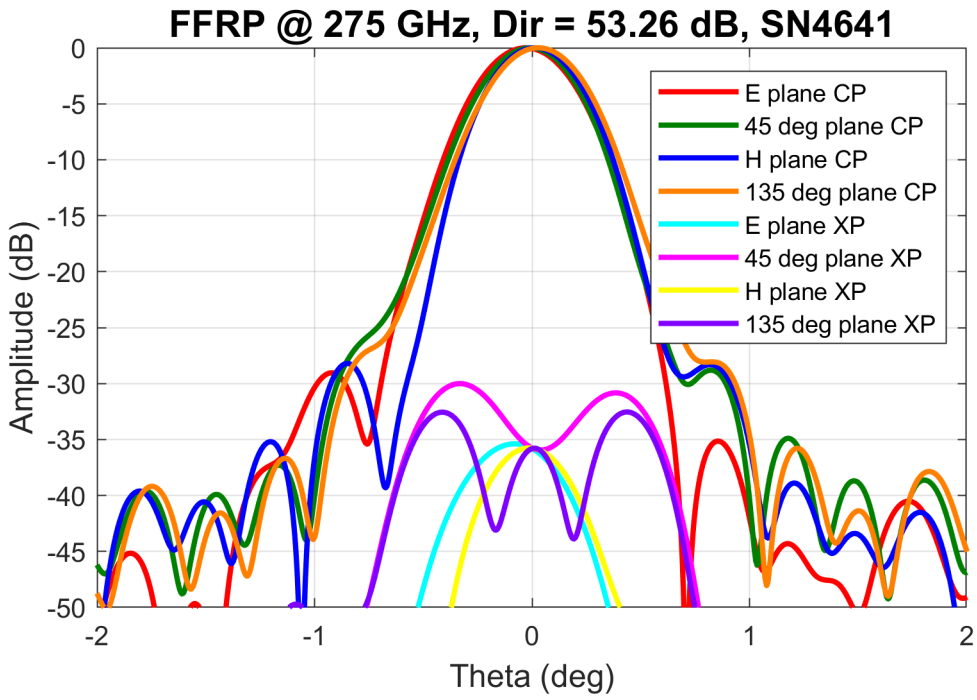

Figure 18. Measured far field radiation pattern at 275 GHz of prototype 1.

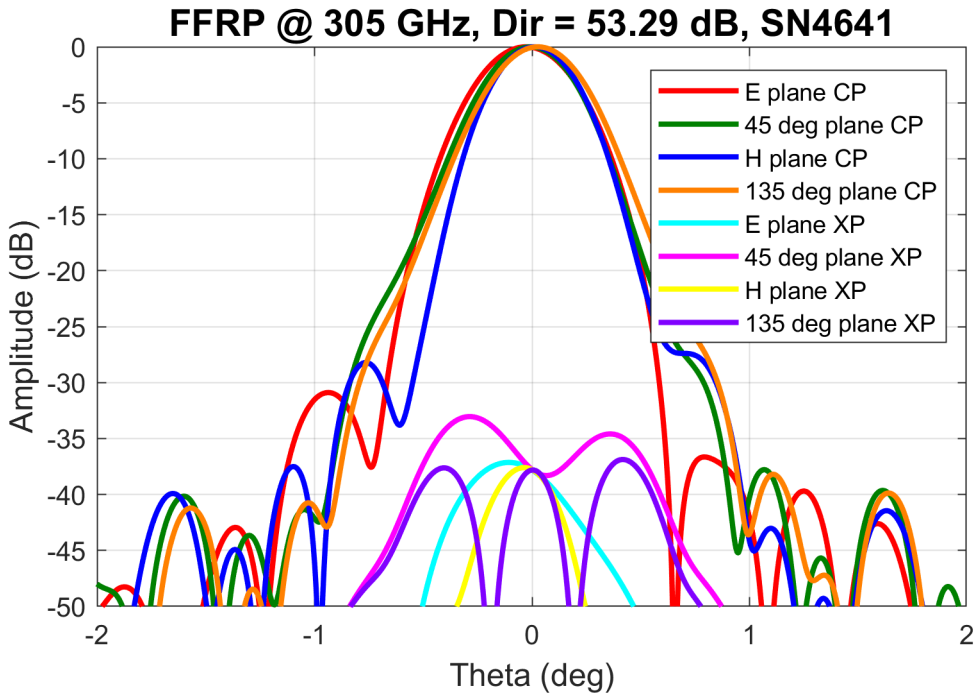

Figure 19. Measured far field radiation pattern at 305 GHz of prototype 1.

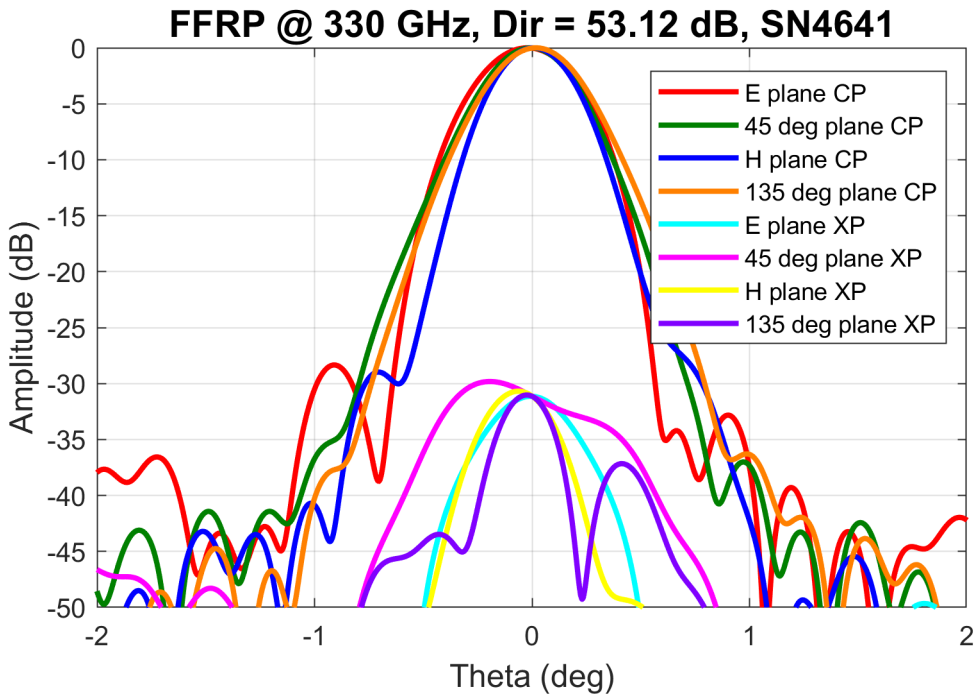

Figure 20. Measured far field radiation pattern at 330 GHz of prototype 1.

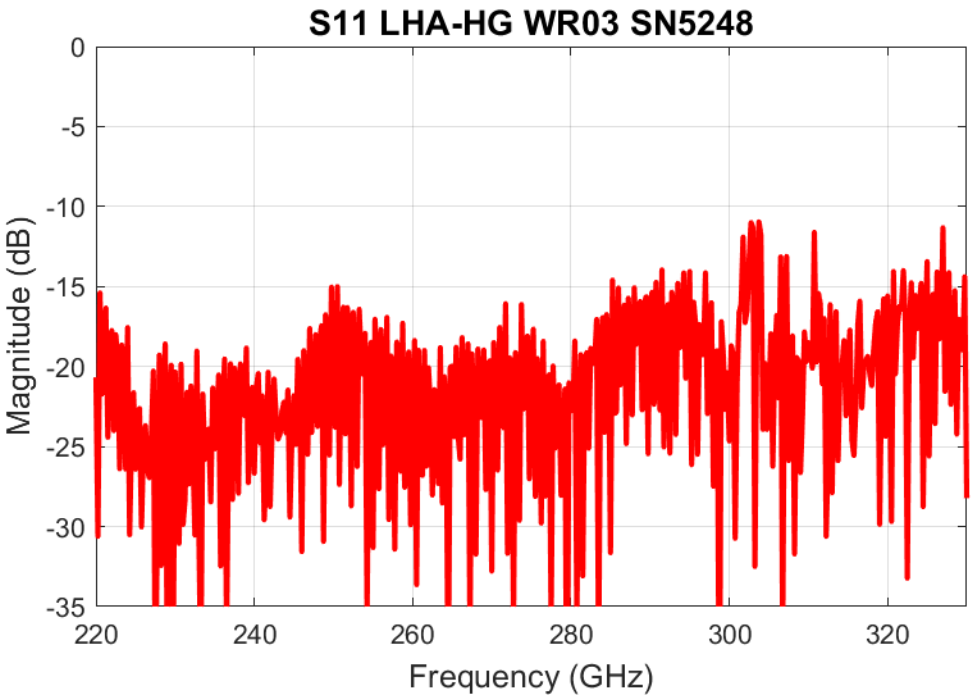

Figure 21. Measured S11 of prototype 2.

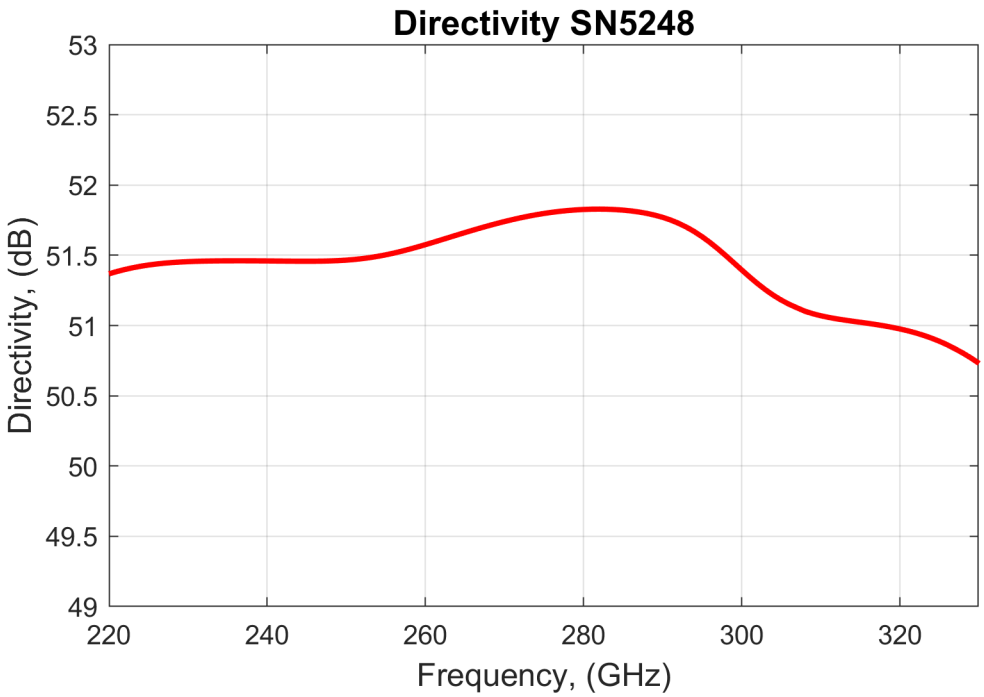

Figure 22. Measured directivity of prototype 2.

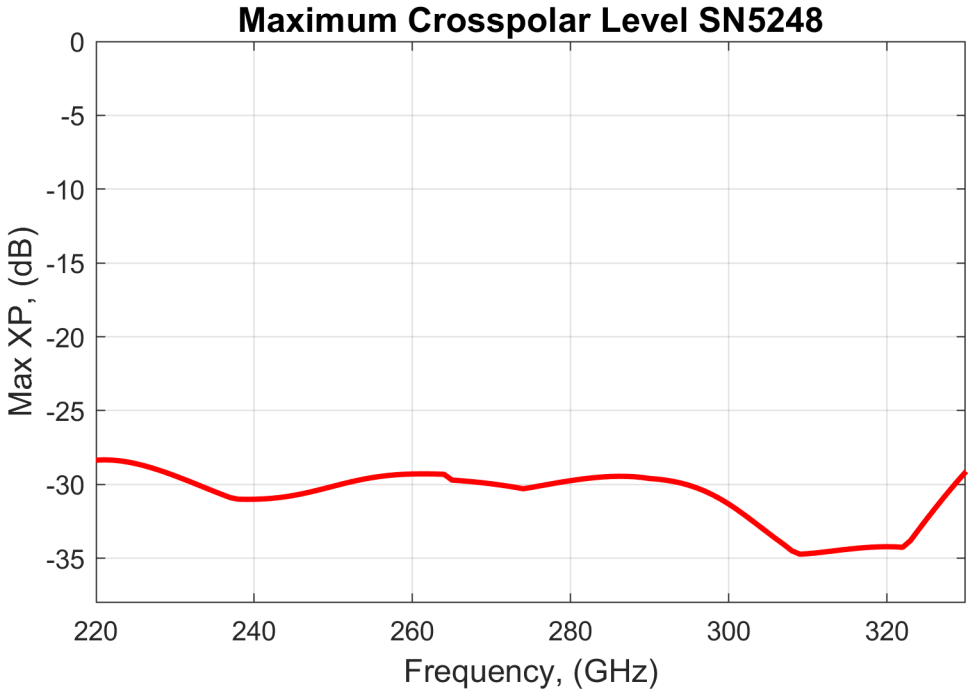

Figure 23. Max. measured crosspolar level of prototype 2.

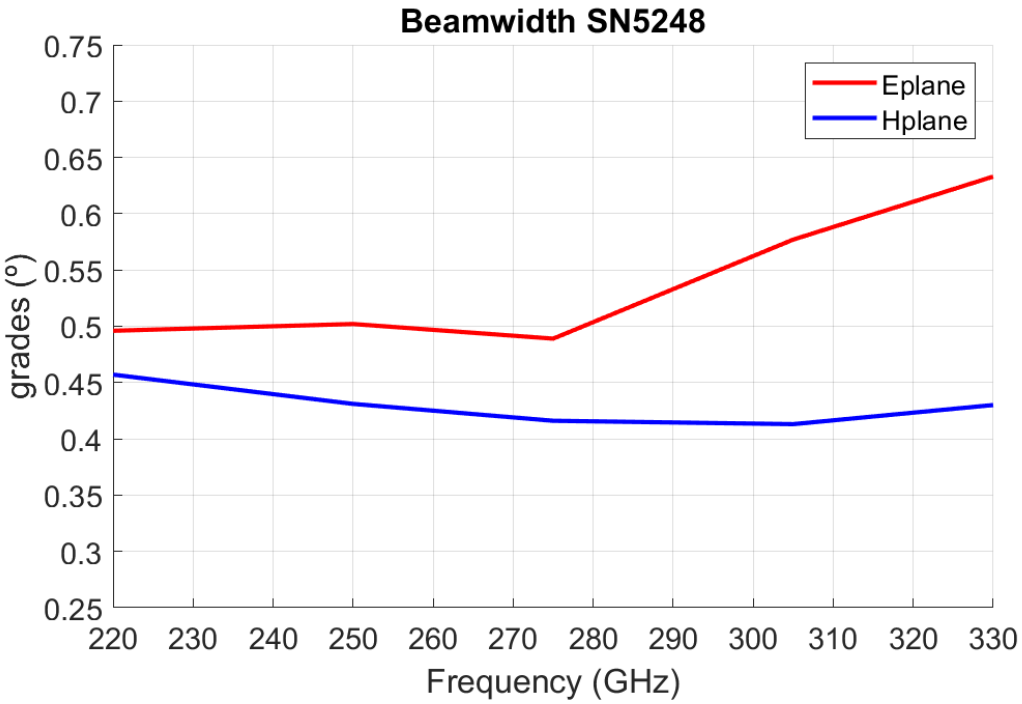

Figure 24. Beamwidth measured of prototype 2.

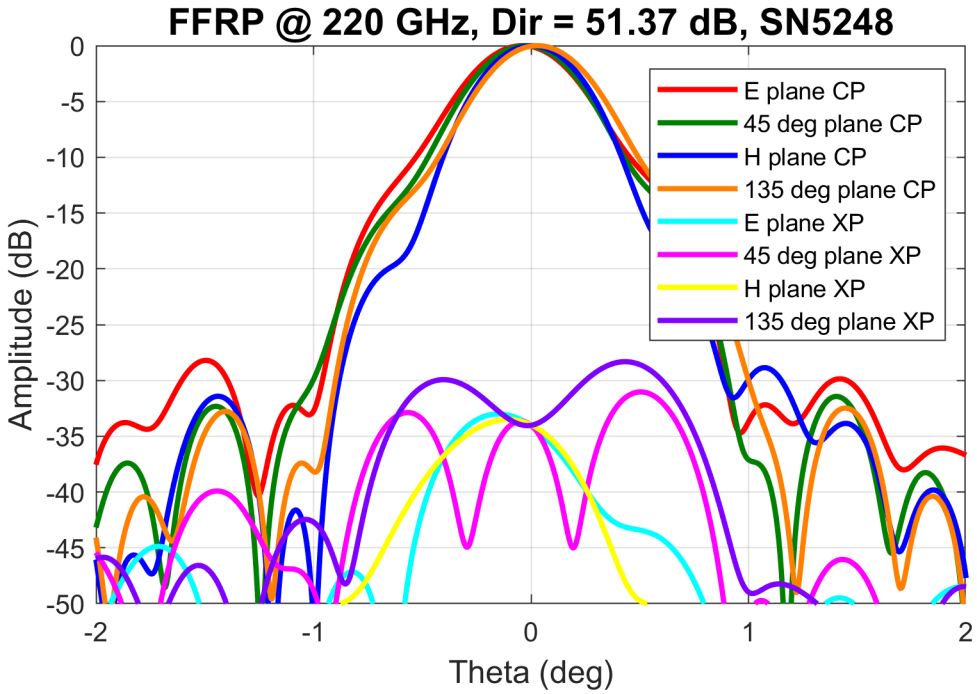

Figure 25. Measured far field radiation pattern at 220 GHz of prototype 2.

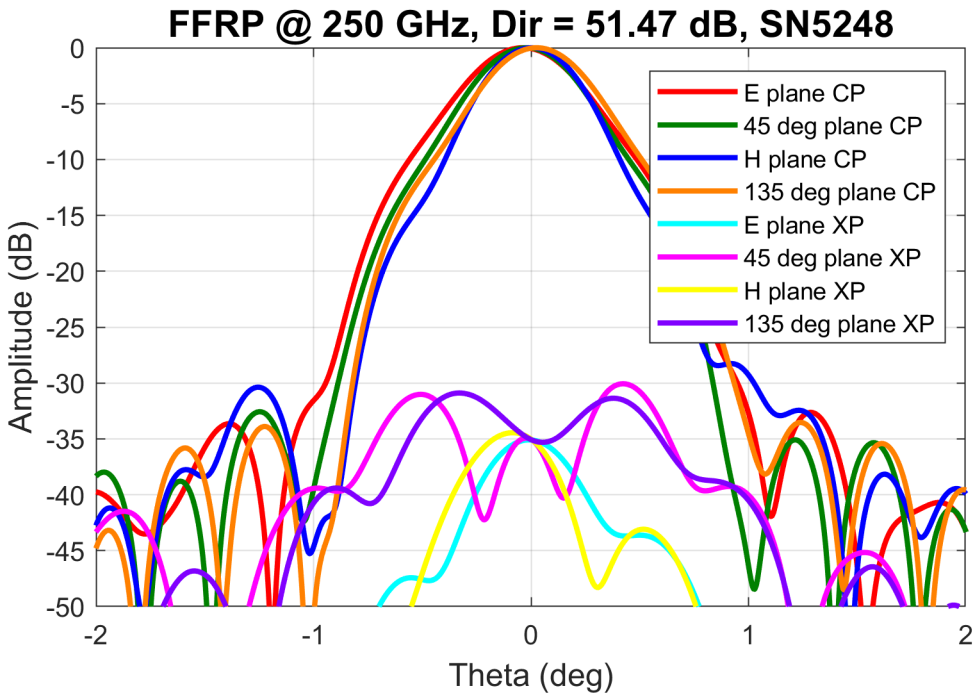

Figure 26. Measured far field radiation pattern at 250 GHz of prototype 1.

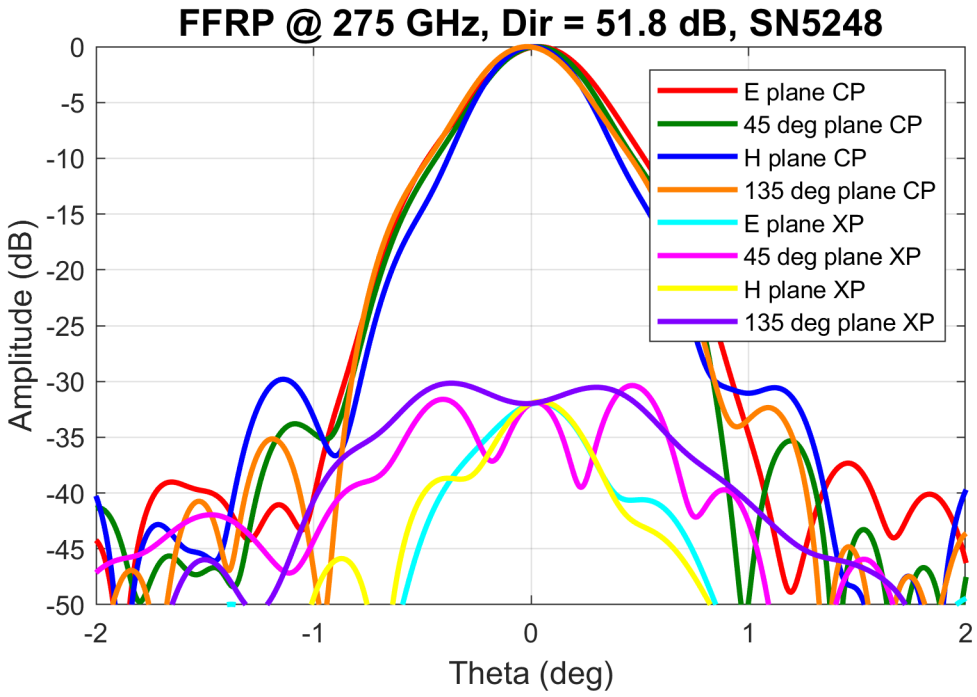

Figure 27. Measured far field radiation pattern at 275 GHz of prototype 2.

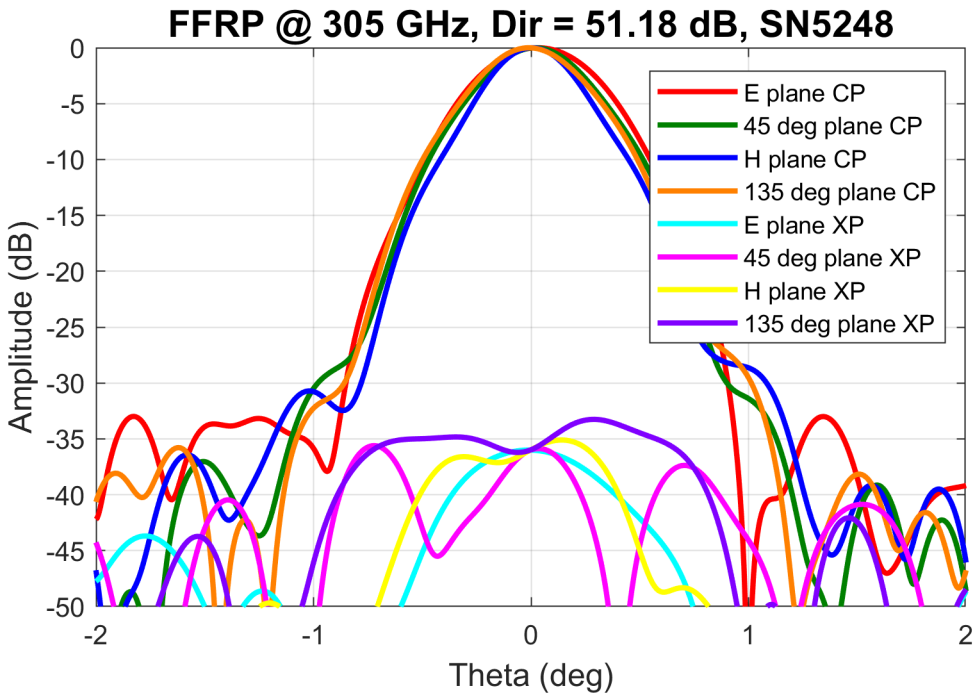

Figure 28. Measured far field radiation pattern at 305 GHz of prototype 2.

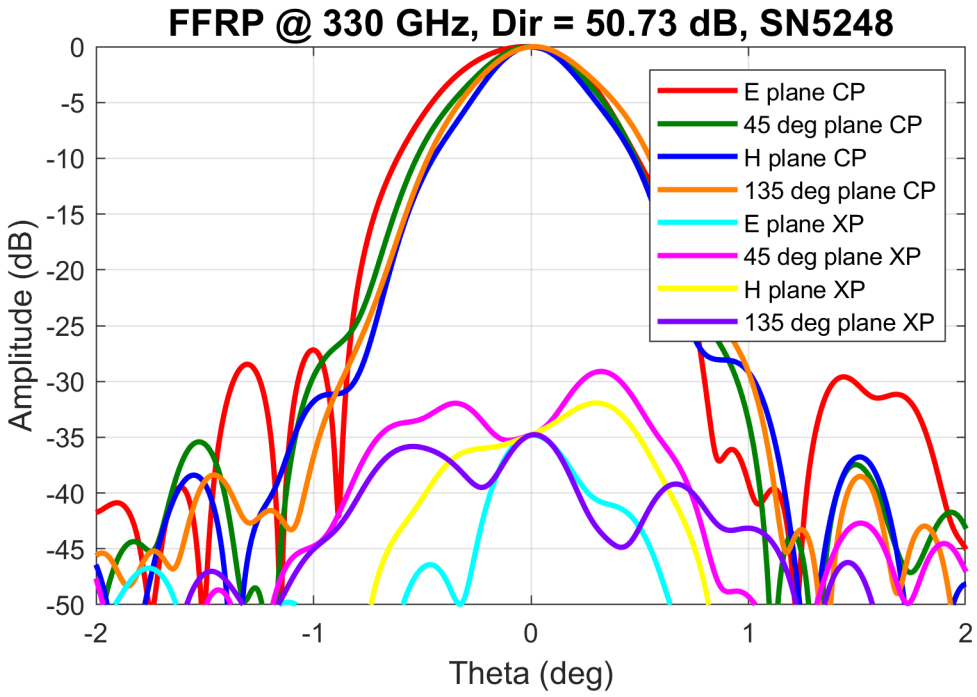

Figure 29. Measured far field radiation pattern at 330 GHz of prototype 2.

The measurement results are highly satisfactory and reflect the good performance of both prototypes. More specifically, in relation to the defined KPIs, the following conclusions can be drawn:

- The return losses are good, as seen in Figures 10 and 19, where the S11 value remains below -10 dB throughout the entire band of interest. The radiated power of the antenna relative to the delivered power is sufficient.
- The directivity exceeds 50 dB across the entire band for both prototypes. Prototype 1 exhibits higher directivity, approximately 1.5 dB at its peak value. Despite being the same manufactured model, this clearly demonstrates that small manufacturing inaccuracies can affect the final performance. At 300 GHz, where the wavelength is 1 mm, manufacturing tolerances must be very small, on the order of tens to a hundred microns.
- Similarly, the beamwidth is less than 0.5 degrees in Prototype 1 and less than 0.65 degrees in Prototype 2. These beamwidth values allow for the calculation of the illumination area for use in the PoCs.
- Although not considered in the KPIs, the cross-polarization component was also measured, showing very good performance in both prototypes, remaining below -25 dB.
- The radiation pattern graphs at different frequencies demonstrate proper beam shaping for all axes in copolar orientation (CP) and cross-polar rejection (XP). The sidelobes range between -25 dB and -30 dB (or better) at all frequencies. In some cases, the -30 dB value defined in the KPI is not fully met, but this is not a critical factor that would prevent the correct operation of the antennas.

The following table shows a summary of the results regarding the KPIs.

Table 2. KPIs requirements and measured results.

KPI	Requirement	Measured Result
Return loss	< -10 dB	< -10 dB at some frequencies < -15 dB at most frequencies
Directivity	> 45 dBi	> 50.5 dBi
Mean beamwidth	< 2 degrees	< 0.65 degrees
Losses	< 1.5 dB	Not measured but < 1.0 dB according simulation
Sidelobe level	< -30 dB	< -25 dB in some frequencies < -30 dB in most frequencies

3.2 Beam steering antennas

3.2.1 Leaky wave antenna

3.2.1.1 Proposed methods for LWA characterization

The proposed testbeds used to characterize the LWA can be divided in two parts:

- To start, VNA measurements are done to analyze the return loss (RL) of the leaky-wave antenna (LWA), then for gain measurement, a reference horn antenna is used at receiver (VNA Port 2), which gain has to be determined.

- Then, a 3D radiation pattern measurement system is used to analyze the LWA output pattern versus frequency.

Detailed description

First a horn conical antenna working in the WR3.4 band is characterized using a testbed on a 220-325 GHz Vector Network Analyzer (VNA) and the gain, depicted in Figure 30), is calculated from S_{21} measurement and the usual Friis equation.

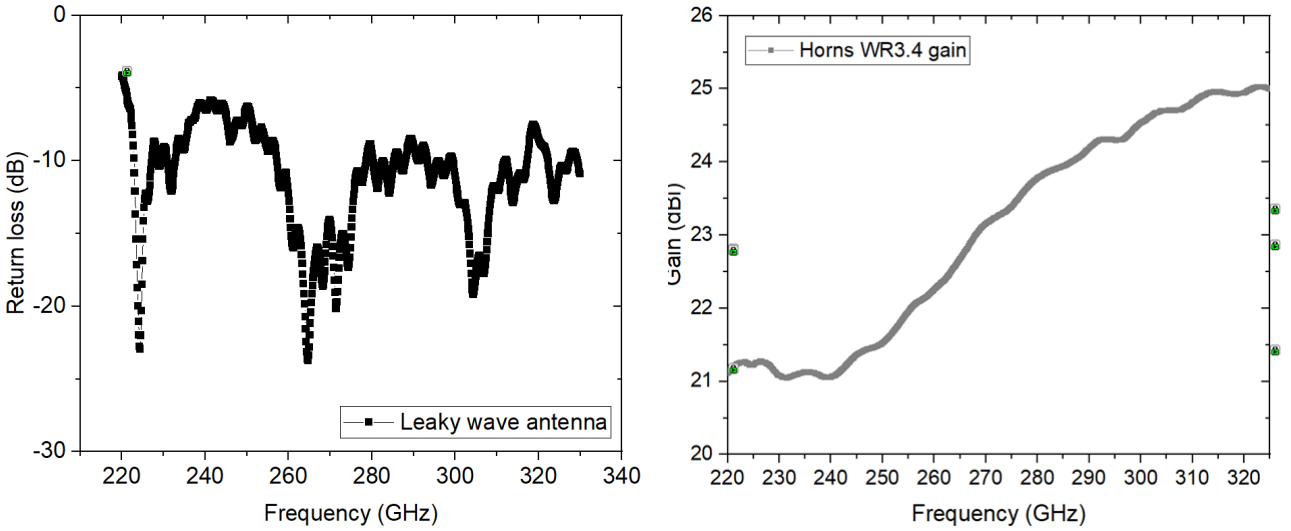

Figure 30. Left: Return loss of the LWA antenna. Right: Horn antenna gain (Horn input is a WR3.4 waveguide).

The radiation pattern testbed (Figure 31) is used is used to obtain the actual gain of the LWA. Here, a reference transmitter is used as an input for the antenna under test (AUT). On the Figure 31, we see the electronic part based on a ×18 multiplier used to feed the waveguide flange of the LWA. In front of Figure 31, the 3D robot system is shown. The receiver is coupled to the reference horn antenna, which was characterized by 220-325 VNA prior to this experiment aforementioned. Then, by moving the 3D robot system on a ½ sphere (one move is displayed in yellow in Figure 31 around the antenna under test (AUT), the gain of the AUT by the horn antenna is obtained thanks to the fixed distance (200 mm) and the calibrated receiver gain.

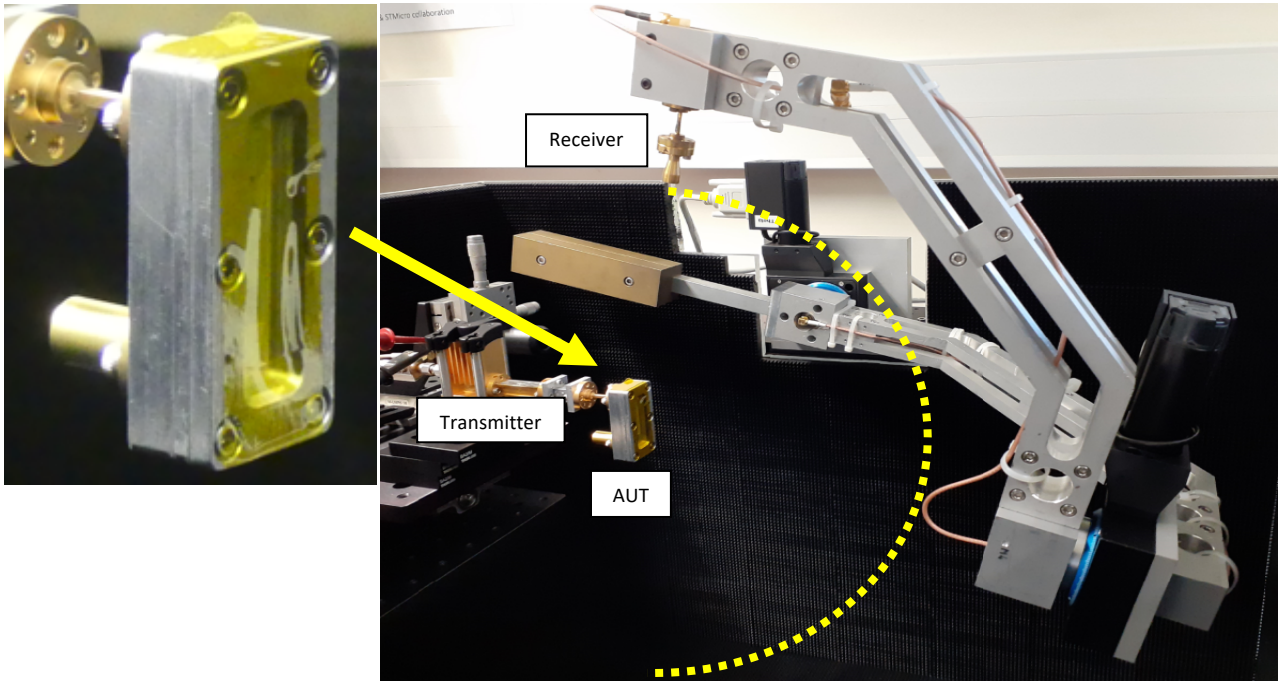

Figure 31. Proposed testbed for antenna characterization (LWA measurement). One trajectory for one angle of the ½ sphere measurement pattern is shown in yellow dashed line.

3.2.1.2 Pattern of the designed LWA

As described in previous sections, the steering capability of the LWA onto the 220-320 GHz frequency band has been simulated and expected to work in the 300 GHz range. By the proposed testbed previously described, the 2D LWA normalized gain pattern is measured for several frequencies in the $\varphi = 0°$ direction. The results are compared with simulations in Figure 32. As it is seen on the figure, the steering capability of the LWA between 50° and 90° is clearly validated for the tested frequencies.

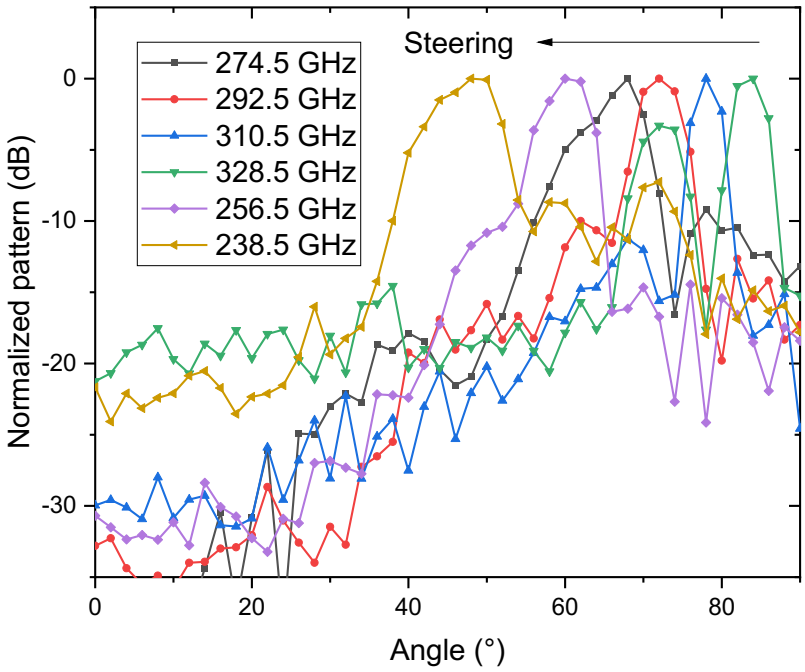

Figure 32. Normalized gain of Leaky Wave Antenna pattern ($\varphi = 0°$) measured.

A 3D scan of the LWA pattern at 274.5 GHz has also been done and is shown in Figure 33. Even though the z-axis is in linear scale, it is clear that the signal coming from the LWA is narrow and almost only directed around 70° even though for less signal, the signal is larger.

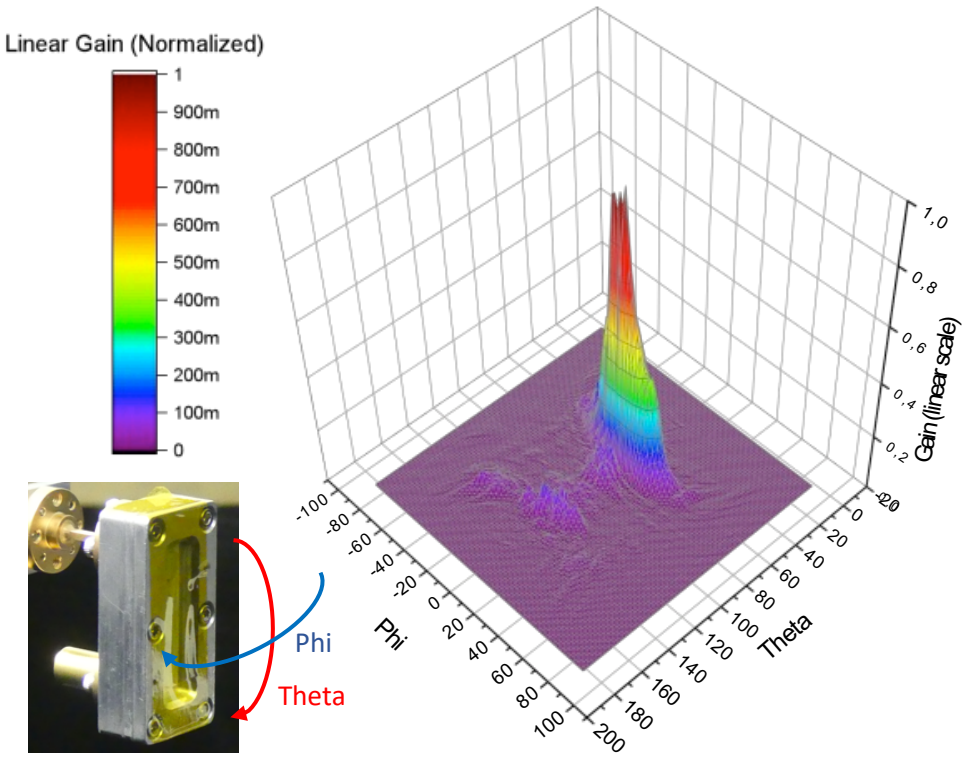

Figure 33. 3D scan of the LWA pattern (in linear scale) at 274.5 GHz.

3.2.1.3 Steering performance

In Figure 34, the steering performance of the LWA is shown. As can be seen from this figure, the agreement of the simulated and measured behavior is reached. However, there is a rough 7~8% shift between simulations and measurements in terms of achieved angle of radiation. It means that for a fixed angle, the LWA radiated the signal with a higher frequency as the one expected from simulations, but the frequency steering of LWA is demonstrated. It doesn't prevent to use it, as the range 260-320 GHz is covered. Looking on the slopes of both curves in the frequency band of main importance, an averaged 0.34°/GHz steering performance is obtained.

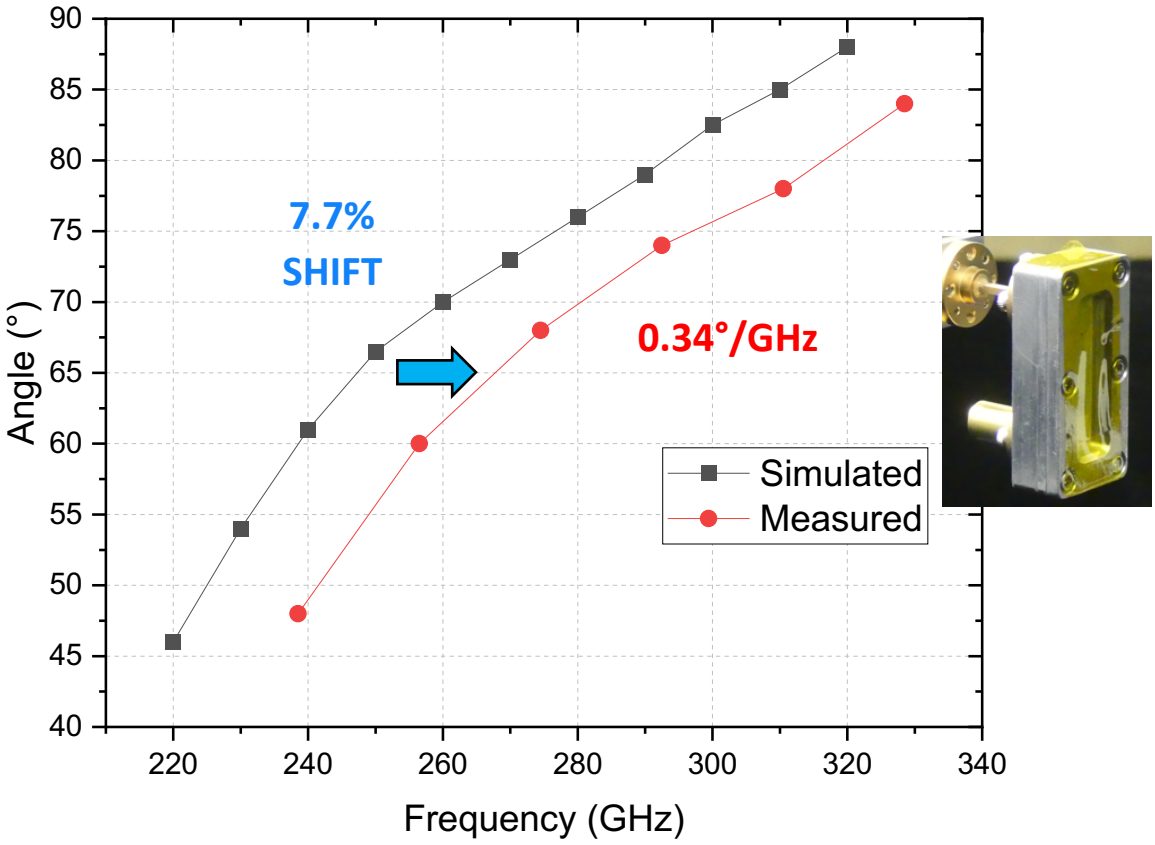

Figure 34. Measured steering performance of the LWA (in red) and comparison with simulations (in black).

3.2.1.4 Measured gain of the designed LWA

As explained in the beginning of this section, the actual LWA gain can be retrieved by comparing the relative gain between the LWA and the Rx horn antenna directly measured from the proposed testbed and the actual horn antenna gain measured by VNA method. The Figure 35 is then obtained by this technique. First, and as it is shown on the figure, a 13 dB difference is seen between measurements and simulations. The impact of side lobes can lead to a reduced gain, and also maybe some RF losses in the structure itself. Compared with simulations, the LWA bandwidth is a bit lower, but a 50 GHz bandwidth on which the LWA gain is higher than 10 dB is clearly seen for measurements.

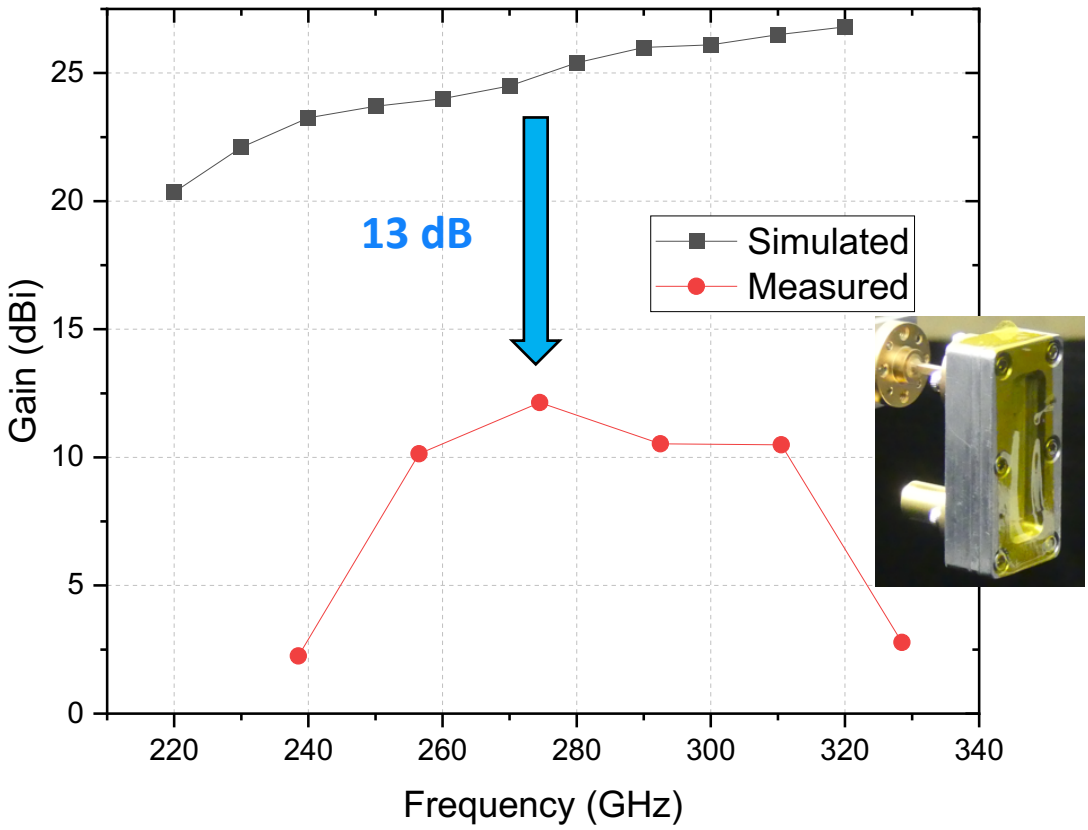

Figure 35. Measured Leaky Wave Antenna gain (in red) and comparison with simulations (in black).

3.2.2 Phase delay line antenna

The proposed testbed used to characterize the Phased Delay Line Antenna (PDLA) is the same as for LWA characterization. Thus, we are going directly into results discussion.

3.2.2.1 Pattern of the designed PDLA

In Figure 36, the normalized gain PDLA pattern in the $\varphi = 90°$ direction is shown. Several comments can be made about this figure. First, as for LWA, the steering performance of the antenna is also confirmed experimentally. Second, for several frequencies, the angular aperture of side lobes seems large and finally, the PDLA response behavior is highly frequency-dependent as it can be seen from the different patterns for different frequencies.

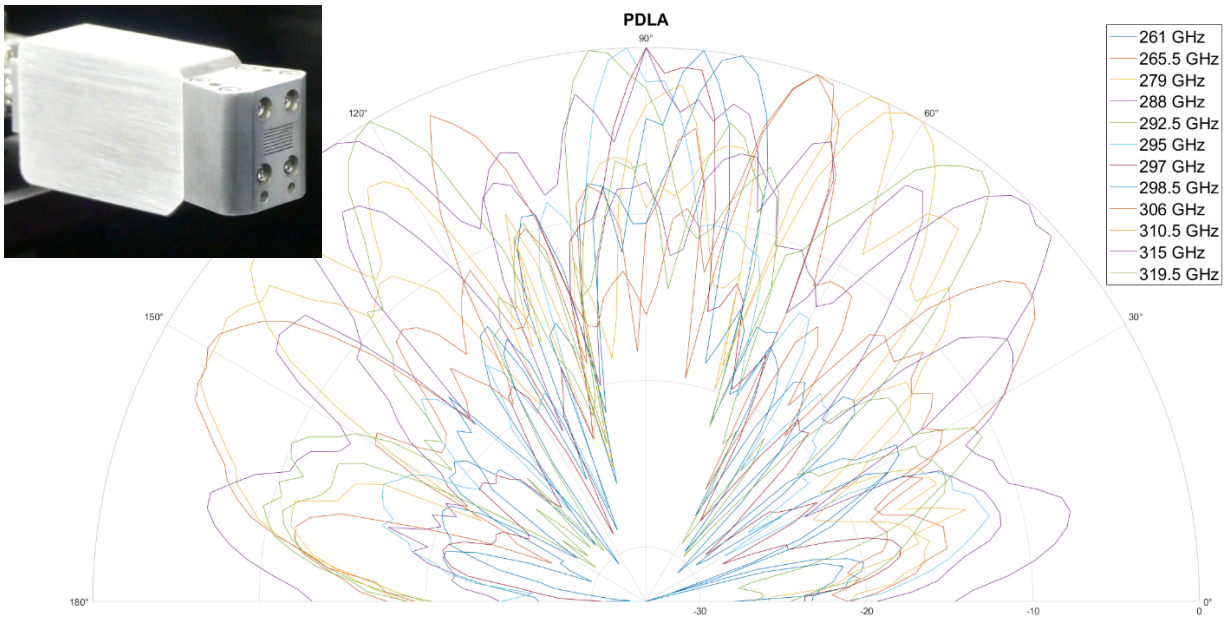

Figure 36. Normalized gain of Phased Delay Line Antenna pattern ($\varphi = 90°$) with respect to the steering angle for each measured frequency. Inset: View of the PDLA fabricated by ANTERAL and measured at CNRS.

In the next figure, selected patterns are also shown for the PDLA:

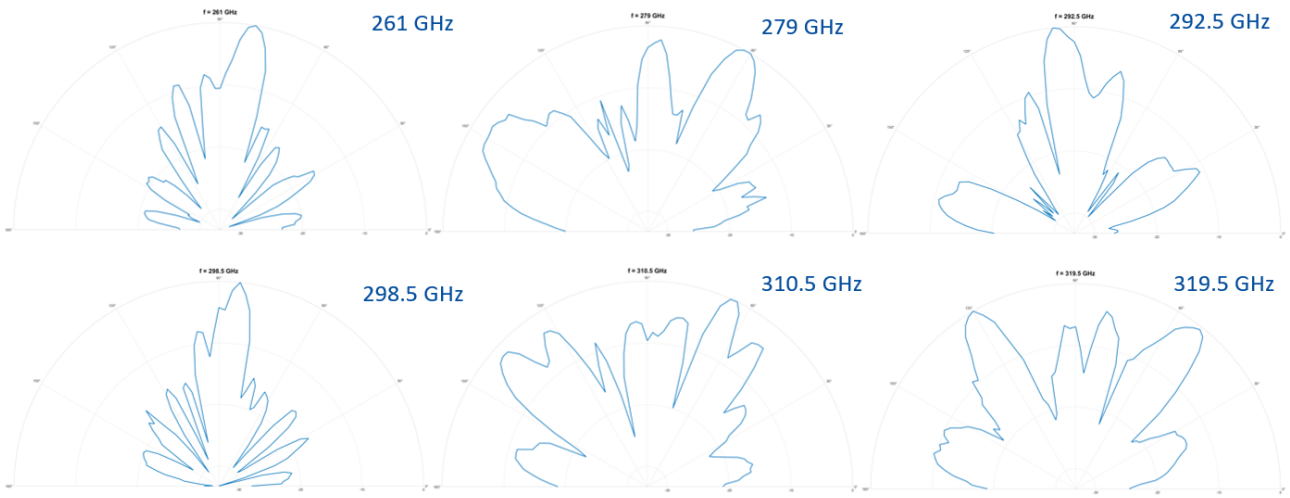

Figure 37. Normalized gain of Phased Delay Line Antenna pattern ($\varphi = 90°$) with respect to the frequency.

3.2.2.2 Antenna Steering performance

In Figure 38, the steering performance of the PDLA is shown. Compared to LWA, in the 280-310 GHz frequency band, measurements are really close to simulations with a very small (0.8%) shift (Red curve). Taking into account of few side lobes, it is still possible to keep the linear behavior of the steering versus frequency (green curve). This linear behavior can be linearly fitted to find a 2°/GHz slope steering performance which is also better than the 0.34°/GHz performance of the LWA.

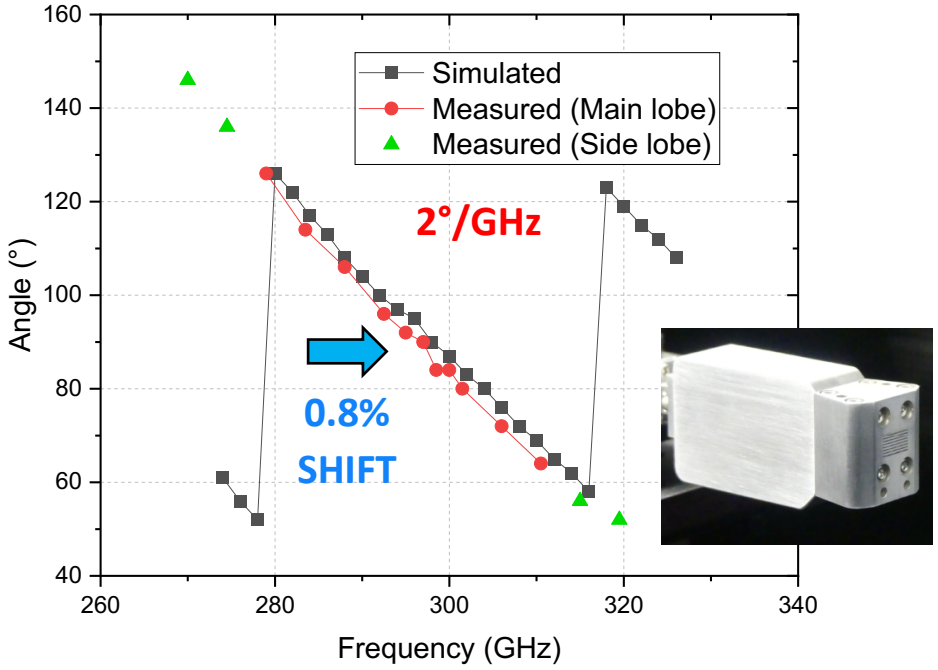

Figure 38. Measured steering performance of the PDLA by taking into account of main lobes (in red) or side lobes (in green) and comparison with simulations (in black).

3.2.2.3 Measured gain of the designed PDLA

As seen from Figure 39, the actual PDLA gain is retrieved by the same method as for the LWA gain. The gain in the $\varphi = 90°$ direction is not as high as in simulations with a 17 dB reduction but the peak at 298 GHz is still well retrieved experimentally. Compared with LWA, in this case, a roughly 7 GHz bandwidth is found with an actual gain higher than 5 dB.

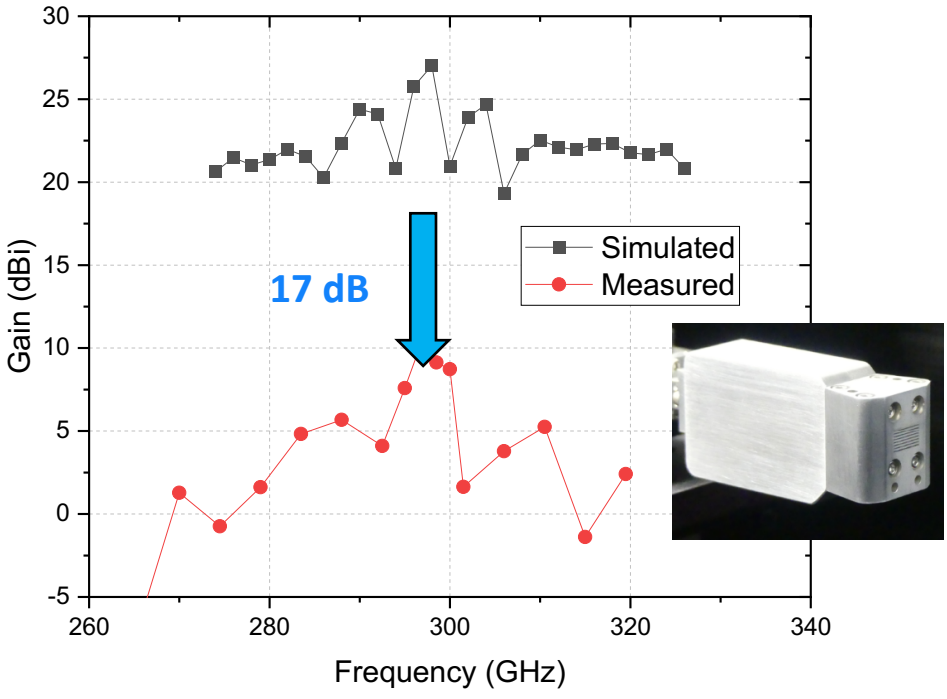

Figure 39. Measured Phased Delay Line Antenna gain (in red) and comparison with simulations (in black).

4 Conclusions

In this section, we summarize the main outcomes of the characterizations and impact to the TIMES PoCs.

IRS

Related to reflective surfaces, 2 designs were proposed, fabricated and characterized. Behavior of the fixed IRS has been verified and confirmed. Methodology of the IRS characterization using VNA technique has been validated, and applied for specular/non-specular response of the IRS. IRS losses of the first 2 prototypes were extracted, with better results for the IRS 2 (fixed one). This surface will be used for the PoC1, for fixed transmission between two points.

Related to the reconfigurable IRS, the device is under characterization at CNRS.

High gain Antennas

- High gain has been achieved in the 300 GHz band, and compliant performances (related to specifications) were achieved. This confirms the PoC1 scenario, with even a bit more margin as antenna gain is a bit higher than expected.

Antennas for THz beam-steering

- LWA and PDLA work as steerable antenna (frequency is the steering parameter).
- Steering behavior is obtained as expected:
  - With a shift for LWA compared to simulations
  - Almost simulated one for PDLA
- Gain performance:
  - Reduced (13 dB) for LWA, 50 GHz bandwidth available with Gain > 10 dB
  - Gain is reducted by ~15 dB from simulations. Gain > 5dB over ~7 GHz

The reduction of the LWA/PDLA antenna gain is probably due to mechanical internal structure of the prototypes and is under investigation at this moment.

Related to the beam-steerable antenna performances, the reduction of the gain will impact the PoC2 link budget, as initial specification was to reach 20 dBi. However, in specific cases an antenna gain at receiver, higher than 20 dBi can compensate a bit the gain reduction of the transmit antenna. However, this is only possible when the receiver direction is corresponding to a circular movement of the robot. The final refinement of the scenario of the PoC2 is still under discussion.

5 References

[1] Antenna Engineering Handbook, (ISBN-13: 978-0071475747).

[2] M. A. Pulido-Gaytán, J. A. Reynoso-Hernández, J. R. Loo-Yau, A. Zárate-de Landa and M. d. C. Maya-Sánchez, "Generalized Theory of the Thru-Reflect-Match Calibration Technique," in IEEE Transactions on Microwave Theory and Techniques, vol. 63, no. 5, pp. 1693-1699, May 2015, doi: 10.1109/TMTT.2015.2417860